# Supporting information for

# Primary Sulfate Is the Dominant Source of Particulate Sulfate During Winter in Fairbanks, Alaska

**Allison Moon**[a*], Ursula Jongebloed[a], Kayane K. Dingilian[b], Andrew J. Schauer[c], Yuk-Chun Chan[a], Meeta Cesler-Maloney[d], William R. Simpson[d], Rodney J. Weber[b], Ling Tsiang[a], Fouad Yazbeck[a], Shuting Zhai[a], Alanna Wedum[a], Alexander J. Turner[a], Sarah Albertin[e], Slimane Bekki[f], Joël Savarino[e], Konstantin Gribanov[g], Kerri A. Pratt[h], Emily J. Costa[h], Cort Anastasio[i], Michael O. Sunday[i], Laura M. D. Heinlein[i], Jingqiu Mao[d], Becky Alexander[a*]

[a] *Department of Atmospheric Sciences and* [c] *Department of Earth and Space Sciences, University of Washington, Seattle, Washington, 98195, United States*

[b] *School of Earth and Atmospheric Sciences, Georgia Institute of Technology, Atlanta, Georgia 30332, USA*

[d] *Department of Chemistry, Biochemistry, and Geophysical Institute, University of Alaska Fairbanks, Fairbanks, AK 99775-6160*

[e] *IGE, Univ. Grenoble Alpes, CNRS, INRAE, IRD, Grenoble INP, 38000 Grenoble, France*

[f] *LATMOS/IPSL, Sorbonne Université, UVSQ, CNRS, 75005 Paris, France*

[g] *Climate and Environment Physics Laboratory, Ural Federal University, 620002, Yekaterinburg, Russia*

[h] *Department of Chemistry & Department of Earth & Environmental Sciences, University of Michigan, Ann Arbor, Michigan 48109 USA*

[i] *Department of Land, Air, & Water Resources, University of California, Davis, CA 95616 United States*

*Email: allimoon@uw.edu, beckya@uw.edu

## TABLE OF CONTENTS

# 1. Experimental methods

## 1.1 Filter sample collection and gas-phase observations in Fairbanks

Prior to the field campaign, filters were soaked for 3 hours in 18 MΩ-cm water with a ratio of 2 liters of water per filter. After soaking, filters were rinsed in a secondary bin before drying completely in a glassware oven at 60°C. Filters were then combusted at 500°C for 8 hours and stored wrapped in aluminum foil in air-tight polyethylene bags.

Exhaust from the TE-5170 was directed through a high-quality HEPA filter located approximately 3 m away from the TE-5170 flow inlet to ensure that its exhaust was not being sampled. The TE-5028 calibration kit with a digital manometer was used approximately every 240 hours of sampling and an $r^2 > 0.99$ was achieved for each flow rate calibration. Before each calibration, 1-min TE-5170 samples with no airflow through the filter were collected and used as blanks for filter analysis. Flow rates ($m^3$/min) were corrected for daily fluctuations in temperature (1-min resolution averaged to 1-hr) and atmospheric pressure (1-min resolution averaged to 1-hr) and used to calculate the total air volume collected for each sample. Size-resolved bins were determined by calculating the particle size cut-off (*Dp,50*) at 50% collection efficiency using the corrected flow rate in each sample (equation S1). Equation S1 shows the calculation of particle size cut-offs:

$$Dp{,}50 = \sqrt{}St \cdot w \cdot \frac{\sqrt{}(9 \cdot n \cdot L)}{C \cdot Pp \cdot Q} \quad \textbf{(S1)}$$

Where *St* is Stoke's number, which depends on jet throat length and jet Reynold's number, *w* is slot width (cm), *n* is gas viscosity ($1.8 \times 10^{-4}$ gm $cm^{-1}$ sec-1 at 25 ˚C, 760 mmHg), *L* is slot length (cm), *Pp* is particle mass density (gm $cc^{-1}$), *C* is cunningham slip correction (*C*=1 for large *Dp*), and *Q* is flow rate (CFM) (Table S1). The average daily flow rate (*Q*) was calculated as the average flow rate per minute multiplied by the number of minutes. The total sample volume that resulted was also used to calculate the ambient concentrations of sulfur species after filter measurement via ion chromatography. Filters were combined to form three-size bins: particles < 0.7 µm ($PM_{0.7}$), 0.7-2.5 µm ($PM_{0.7-2.5}$), and 2.5-10 µm ($PM_{2.5-10}$) (Figure S1).

**Table S1.** Particle size cut-off variables used in equation S1

| Stage | St | W | n | L | Pp | C |
|---|---|---|---|---|---|---|
| 1 | 0.6 | 0.396 | 0.00018 | 11.049 | 1 | 1.02 |
| 2 | 0.58 | 0.163 | 0.00018 | 13.77 | 1 | 1.06 |
| 3 | 0.52 | 0.0914 | 0.00018 | 12.3952 | 1 | 1.11 |
| 4 | 0.69 | 0.0457 | 0.00018 | 12.3952 | 1 | 1.17 |

In-situ gas phase $SO_2$ (Thermo Scientific 43C) and $O_3$ (Thermo Scientific 49C) were measured from an inlet at 3m above the valley floor at the CTC site. The in-situ analyzers were both calibrated roughly weekly using an EPA certified mixed standard of 5.190 millimol $mol^{-1}$ $SO_2$ that was diluted with an Environics 9100 calibration system to cover the ambient $SO_2$ mixing ratio range (from zero to ~125 nmol $mol^{-1}$). The same calibrator generated $O_3$ for calibration of the $O_3$ analyzer (from zero to ~200 nmol $mol^{-1}$). Calibration standard gases were diluted in zero air and were delivered to the instruments at overflow during multi-point calibrations. The average instrument zero and a zero-intercept linear correlation slope were determined for each calibration and linearly interpolated temporally between calibrations as correction factors for the raw instrument measurements.

### 1.2 Ion chromatography to measure HMS, non-HMS S(IV) and $SO_4^{2-}$

Recent work has shown that hydroxymethanesulfonate (HMS) can contribute 25-30% of total sulfur by mass in cold, dark, and polluted conditions, and may have been mistaken for sulfate.[1–3] This is because most ion chromatography and mass spectrometry methods cannot tell HMS, non-HMS S(IV), and $SO_4^{2-}$ apart due to instability in solution and matrix effects between sulfur species.[4–7] At pH > 6, HMS decomposes into sulfite and is rapidly oxidized to form sulfate.[1,3,6] This creates a positive measurement bias for sulfate in ion chromatographic methods with strongly basic eluents (e.g., KaOH, NaOH).[6]

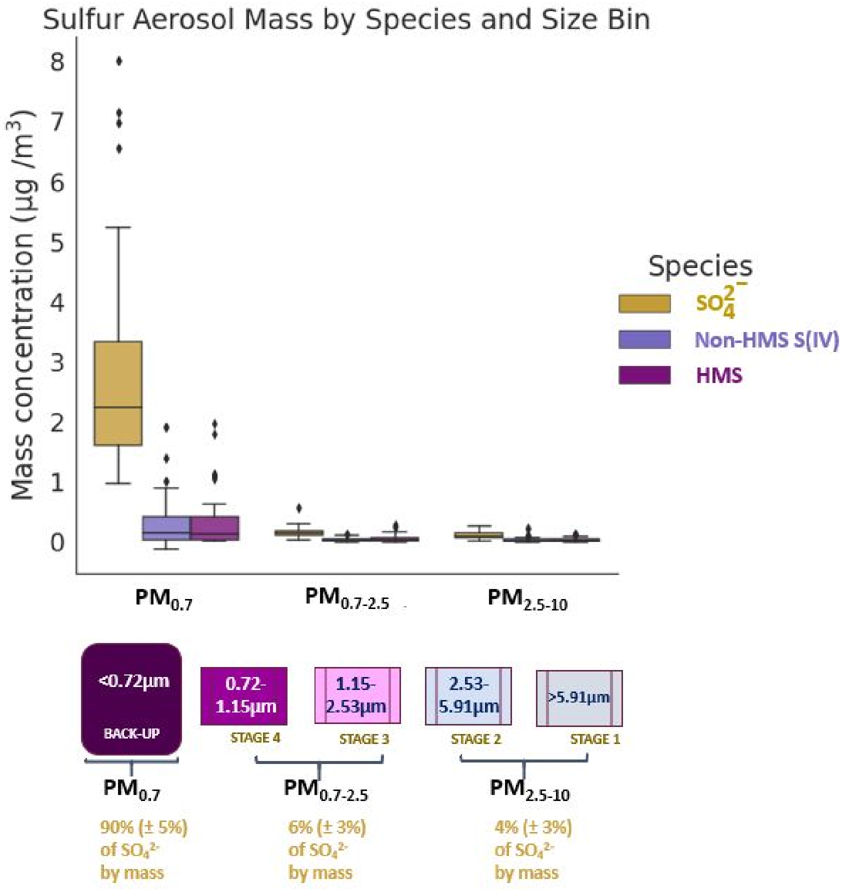

**Figure S1.** Average size cut-offs for the 4-stage cascade impactor and back-up filter. Filters were grouped into three size bins for isotope measurements: $PM_{0.7}$ for PM < 0.7μm (left), $PM_{0.7\text{-}2.5}$ for 0.7 < PM < 2.5μm (middle), and $PM_{2.5\text{-}10}$ for PM > 2.5 μm (right). Size resolved boxplots of $SO_4^{2-}$ (gold), non-HMS S(IV) (blue), and HMS (purple) mass concentrations are shown along with outliers plotted as black diamonds.

**Table S2: Sampling periods for $PM_{0.7\text{-}2.5}$ and $PM_{2.5\text{-}10}$ size bins**

| Period | Sample duration | Start date (MM/DD/YY) and local time | Stop date (MM/DD/YY) and local time |
|---|---|---|---|
| Period 1 | 24 hr | 01/17/22 2:00 pm | 01/24/22 9:00 am |
| Period 2 | 24 hr | 01/24/22 9:30 am | 01/29/22 9:00 am |
| Period 3 Polluted day | 8 hr | 01/29/22 9:30 am | 02/02/22 5:00 pm |
| Period 4 Polluted night | 16 hr | 01/29/22 5:30 pm | 02/03/22 9:00 am |
| Period 5 | 24 hr | 02/03/22 9:30 am | 02/06/22 9:00 am |
| Period 6 | 24 hr | 02/06/22 9:30 am | 02/09/22 9:00 am |
| Period 7 | 24 hr | 02/09/22 9:30 am | 02/13/22 9:00 am |
| Period 8 | 24 hr | 02/13/22 9:30 am | 02/17/22 9:00 am |
| Period 9 | 24 hr | 02/17/22 9:30 am | 02/18/22 9:00 am |
| Period 10 | 24 hr | 02/21/22 9:30 am | 02/26/2022 9:00 am |
| PF220208 | 7 days | | |
| PF220221 | 7 days | | |

Dates of blanks collection (MM/DD/YY): 01/25/22, 02/02/22, 02/8/22, 02/20/22.

## 1.3 Isotopic analysis

### 1.3.1 Oxygen isotope measurements

For isotope analysis at the University of Washington IsoLab, filter samples (including blank filters collected in Fairbanks) were extracted into 18 MΩ-cm water and then filtered through a 0.2μm Polyethersulfone (PES) syringe filter to remove insoluble species. The filtrate was neutralized by converting the anions to sodium-form with an offline cation-exchange resin (AG 50W-X8 Resin from Bio-Rad) before removing organics from the sample matrix by adding 30% $H_2O_2$ and drying in a MiVac Duo concentrator as described in Schauer et al. (2012).[8] To isolate sulfate ions from the inorganic mixture, samples were rehydrated and pre-concentrated in a Dionex 4 x 50mm Ionpac AS19 guard column before being pumped into a Dionex ICS-2000 as described in Geng et al. (2013).[9] A 60-minute multi-step eluent gradient of KOH (5mM, 10mM, 15mM, 25mM) separated anions through a 4mm Dionex IonPac AS19 analytical column and Dionex ADRS 600 4mm suppressor at a flow rate of 1 mL/min. Sulfate fractions were isolated with a Foxy

Jr. fraction collector using automated peak detection software. Blanks received identical treatment in all sample preparation through the ion separation step. Sulfate measured in the Dionex ion chromatograph for the blank filters collected in Fairbanks was far below the detection limit for both mass spectrometers, suggesting that any minor contamination of sulfate during sample preparation could not alter the isotopic composition of the samples.

All isotope samples were prepared for silver salt pyrolysis using $Ag^+$-charged cation-exchange resin to convert sulfate to $Ag_2SO_4$, as described in Geng et al. (2013).[9] Sulfur and oxygen isotope measurements were obtained by splitting each sample into two separate containers, silver capsules for sulfur isotopes and quartz cups for oxygen isotopes, drying the samples in the capsules to form solid $Ag_2SO_4$, and measuring both on the same day. Oxygen isotope measurements were performed on a Finnegan MAT 253 isotope ratio mass spectrometer using the silver salt pyrolysis technique as detailed in Schauer et al. (2012) and Geng et al. (2013).[8,9] Briefly, $Ag_2SO_4$ in quartz capsules is pyrolyzed at 1000˚C in a Temperature Conversion/Elemental Analyzer (TC/EA) with a helium gas carrier flow rate of 30 mL/min to form Ag(s), $SO_2$(g), and $O_2$(g). $SO_2$ gas is sequestered in a stainless-steel trap submerged in liquid nitrogen while non-condensable gasses are separated with a 3-m gas chromatography column. A substantial flow rate reduction in a gasbench allows for *m/z* isotope measurements of $^{32}O_2$, $^{33}O_2$, and $^{34}O_2$ gas following VSMOW-calibrated reference gas measurements prior to every sample peak. $\delta^{18}O$ and $\delta^{17}O$ are calculated as:

$$\delta^{x}O = \frac{R^{x}_{SA}}{R^{x}_{VSMOW}} - 1 \tag{2}$$

where $R^{x}_{SA}$ is the ${}^{x}O/{}^{16}O$atomic abundance ratio of the sample, $R^{x}_{VSMOW}$ is the same ratio of Vienna Standard Mean Ocean Water (VSMOW), and x = 17 or 18. $\Delta^{17}O$ is calculated with equation 1 in the main text. $\delta^{18}O$ and $\Delta^{17}O$ measurements obtained in quartz capsules were corrected for isotopic exchange with quartz using known values for oxygen isotope exchange during pyrolysis, which was constrained in prior work by Schauer et al. (2012) and replicated here (equations S3 and S4 from Figure S2).

$$\delta^{18}\mathrm{Ogold} \; = \; (\delta^{18}\mathrm{Oquartz} * 1.06) - 1.00 \tag{3}$$

$$\Delta^{17}\mathrm{Ogold} \; = \; (\Delta^{17}\mathrm{Oquartz} * 1.18) + 0.06 \tag{4}$$

$$\text{where } (\Delta^{17}\mathrm{Oquartz} \; = \delta^{17}\mathrm{Oquartz} - 0.52 * \delta^{18}\mathrm{Oquartz})$$

Isotope standards included an IAEA-N-1 stable isotope reference material for $\delta^{18}O$, an isotopically uniform selenite sample, three inter-laboratory calibrated $\Delta^{17}O$ standards (Sulf-α, Sulf-β, and Sulf-ε), and five newly synthesized standards (s-bravo, s-charlie, s-delta, s-echo, and s-foxtrot) prepared at the University of Washington.[9] The five new standards were synthesized to replenish supply of standards and are published here for posterity. Five new standards (s-bravo, s-charlie, s-delta, s-echo, and s-foxtrot) were synthesized and incorporated in the quartz capsule corrections for the $\delta^{18}O$ and $\Delta^{17}O$ measurements. Briefly, 12.5 g of reagent $Na_2SO_3$ was dissolved in a 100 mL volumetric flask with 3.5, 7.5, 12, 25, and 50 mL of $^{17}O$-enriched water (20 µL of 90% $^{17}O$ water diluted to 1 L from Cambridge Isotope Laboratories, Andover, MA, USA), respectively. Solutions were left to equilibrate overnight before $H_2O_2$ was added the next afternoon in a fume hood. Solutions were stirred in a fume hood for 24 hours and placed in a 60°C oven until all water evaporated and the product $Na_2SO_4$ was crystallized. Standards were ground with a mortar and pestle and stored in a desiccator. The measured $\delta^{18}O$ and $\Delta^{17}O$ values in quartz and gold are shown in Table S3 A correction for oxygen isotopic exchange with quartz was performed for the raw measured values of $\delta^{18}O$ using 11 standards analyzed in both quartz and gold cups (Figure S2). The new corrections for isotopic exchange with quartz compared well with previous values from Schauer et al. (2012) and are plotted together in figure S2(a-b).[8]

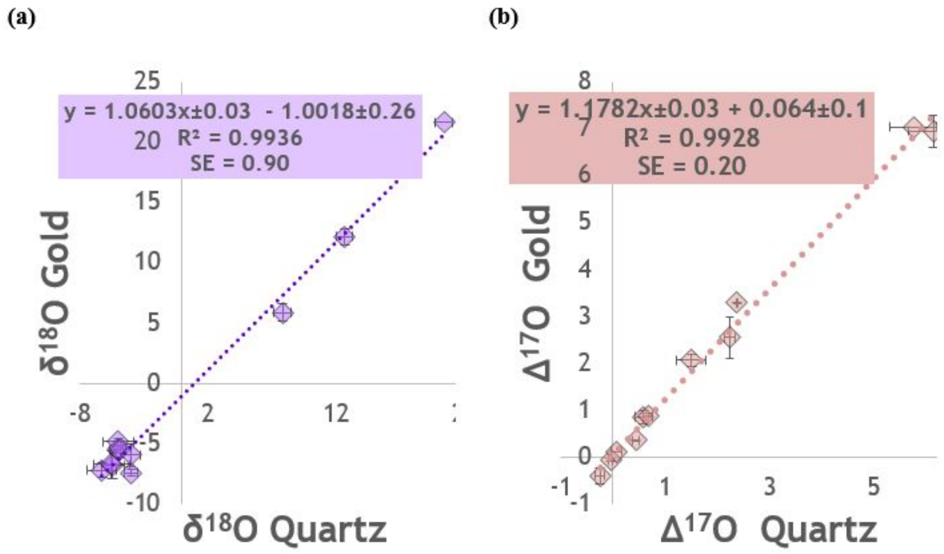

**Figure S2(a)** Average $\delta^{18}O$ measurements in quartz and gold capsules for each standard. The regression equation used for $\delta^{18}O$ quartz correction is shown in inset. **(b)** Average $\Delta^{17}O$ measurements in quartz and gold capsules for each standard. The regression equation used for $\Delta^{17}O$ quartz correction is shown in inset.

**Table S3.** Average measured $\delta^{18}O$ and $\Delta^{17}O$ values for standards and one sample used for corrections for oxygen isotopic exchange with quartz during $Ag_2SO_4$ pyrolysis.

| Standard | $\delta^{18}O_{quartz}$ (±σ) | $\delta^{18}O_{gold}$ (±σ) | $\Delta^{17}O_{quartz}$ (±σ) | $\Delta^{17}O_{gold}$ (±σ) |
|---|---|---|---|---|
| **sulf-alpha** | -6.25 (±1.2) | -7.16 (±0.60) | 0.59 (±0.16) | 0.86 (±0.15) |

| | | | | |
|---|---|---|---|---|
| **sulf-beta** | -5.41 (±0.90) | -6.78 (±1.1) | 1.5 (±0.28) | 2.07 (±0.12) |
| **sulf-epsilon** | -5.52 (±1.40) | -6.71 (±1.2) | 5.76 (±0.44) | 7.04 (±0.17) |
| **selenite** | 12.65 (±0.66) | 12.18 (±0.66) | -0.04 (±0.04) | -0.06 (±0.04) |
| **IAEA-N-1** | 7.83 (±0.68) | 5.88 (±0.73) | -0.25 (±0.09) | -0.39 (±0.18) |
| **s-bravo** | -4.97 (±1.23) | -4.83 (±0.29) | 0.44 (±0.07) | 0.36 (±0.01) |
| **s-charlie** | -4.98 (±0.62) | -5.48 (±0.31) | 0.67 (±0.09) | 0.89 (±0.04) |
| **s-delta** | -3.95 (±0.51) | -7.39 (±0.24) | 2.24 (±0.11) | 2.55 (±0.45) |
| **s-echo** | -4.81 (±0.21) | -5.44 (0.67) | 2.38 (±0.02) | 3.29 (±0.05) |
| **s-foxtrot** | -4.01 (±0.77) | -5.89 (±0.94) | 6.14 (±0.46) | 6.95 (±0.34) |
| **A220130** | 20.41 (±0.68) | 21.65 | 0.07 (±0.1) | 0.12 |

### 1.3.2 Sulfur isotope measurements

Sulfur isotope composition ($^{64}SO_2$ and $^{66}SO_2$) was measured using a separate Finnegan MAT 253 isotope ratio mass spectrometer with the same configuration as Jongebloed et al. (2023).[10] To optimize combustion yield, the silver capsules were folded and packed with vanadium pentoxide and elemental tin powder before being converted to $SO_2$(g) in the Thermo Scientific high-temperature conversion elemental analyzer (TC/EA). $\delta^{34}$S is calculated as:

$$\delta^{34}S = \frac{R_{SA}^{34}}{R_{VCDT}^{x}} - 1 \qquad \textbf{(5)}$$

where $R_{SA}^{34}$ is the $^{34}S/^{32}S$ ratio of the sample, $R_{VCDT}^{x}$ is the same ratio of Vienna Canyon Diablo Troilite (VCDT). $\delta^{34}$S values were normalized to the VCDT scale using four in-house reference materials that are regularly calibrated against the international reference materials IAEA-S-1, IAEA-S-3, and NBS-127. The analytical error of the measurements estimated from duplicate sample analysis (performed on 30% of Fairbanks samples) and replicate measurements of standards in quartz and silver capsules was: ± 0.6‰, ± 0.2‰, and ± 0.8‰ for $\delta^{18}$O, $\Delta^{17}$O, and $\delta^{34}$S, respectively. The fully propagated error including isotopic corrections for the three measurements are as follows: $\delta^{18}$O (± 1.9‰), $\Delta^{17}$O (± 0.4‰), and $\delta^{34}$S (± 1.2‰).

Sulfur isotopic composition of residential home heating oils #1 and #2 purchased in Fairbanks was measured using the configuration from Jongebloed et al. (2023) with one modification: vanadium pentoxide was not packed in the tins with the sample because the fuel oil did not need an additional oxygen source.[10] 6μL of fuel oil was added to a 50 μL tin capsule packed with tin powder. Caution should be used when measuring $\delta^{34}S(S)$ using this method because fuel oil is flammable, resulting in explosive combustion in the TC/EA. . $\delta^{34}S(S)$ values are reported in Table S4 along with the fractional use of each fuel type in FNSB and the sulfur content of both heating oils. This yields a $\delta^{34}S(S)$ signature of 4.7±0.6‰, which was used as an emissions signature in the isotope mixing model.

**Table S4. $\delta^{34}S(S)$ measurement of Fairbanks fuel oil**

| Fuel oil Type | Sulfur content (ppmv) | Quantity of fuel oil combusted | Fraction of total fuel oil used in Fairbanks (ADEC, 2019) | Estimated contribution to fuel oil-derived sulfur based on sulfur content and domestic use | Measured $\delta^{34}S(S)$ | **Weighted average $\delta^{34}S(S)$** |
|---|---|---|---|---|---|---|
| Fuel oil #1 | 896 | 6 μL | 33% | 15% | 3.7±0.6‰ | **4.7±0.6‰** |
| Fuel oil #2 | 2,566 | 6 μL | 67% | 85% | 4.9±0.1‰ | |

## 1. 4 HMS and non-HMS S(IV) correction for $\delta^{18}O$, $\Delta^{17}O$, and $\delta^{34}S$ isotope measurements

### 1. 4.1 HMS and non-HMS S(IV) correction for oxygen isotopes

HMS decomposes in non-acidic conditions and thus during ion chromatography using basic eluants (e.g., KOH as used in this study).[1,6,11] Prior to the ion chromatography step, HMS is known to decompose to formaldehyde and bisulfite during sample storage and as it is extracted in water in an equilibrium reaction (scheme 1 from Figure S3).[1,2,6] Furthermore, in this method, the sample matrix is immediately neutralized in the offline cation-exchange step by stripping the anions of hydrogen ions and replacing them with sodium ions (section I.3). The 60-minute multi-step eluent gradient of KOH (5mM, 10mM, 15mM, 25mM) used in the IC separation step further induces HMS decomposition.

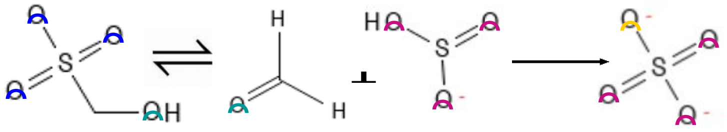

$$HOCH_2SO_3 \rightleftharpoons HCHO + (H)SO_3^- \rightarrow SO_4^{2-}$$ **(Scheme 1)**

**Figure S3.** Decomposition of hydroxymethanesulfonate ($HOCH_2SO_3$) during sample preparation. HMS formed in Fairbanks has three oxygens from dissolved S(IV) (blue) and one oxygen from HCHO (green). S(IV) formed during decomposition of HMS in the laboratory equilibrates with laboratory water (pink) before it obtains its forth oxygen (yellow) from either dissolved $O_2$ or $H_2O_2$, depending on when the HMS decomposes (before or after addition of $H_2O_2$).

Laboratory experiments were performed to determine whether the neutralization step induces further HMS decomposition in addition to the IC separation step first observed by Dovrou et al (2019).[6] Three solutions were tested: 100% HMS (2µmol HMS dissolved in 10mL Milli-Q), 50% HMS, 50% $Na_2SO_4$ (1µmol HMS + 1µmol $Na_2SO_4^{2-}$ dissolved in 10mL Milli-Q), and 100% SO4 (2µmol $Na_2SO_4^{2-}$ dissolved in 10mL Milli-Q). The neutralized samples were prepared by dissolving the reagents $HOCH_2SO_3Na$ and $Na_2SO_4$ in laboratory water, converting the solutions to sodium form as described in section S1.3, and then measuring them on the IC with the 60-minute multi-step eluent gradient detailed above. The non-neutralized samples were prepared by dissolving the reagents and measuring them on the IC with the same eluent gradient but without the neutralization step. Solution preparation and IC measurement were performed on the same day to be consistent with field sample extraction. The percent yield of sulfate formed from decomposition of HMS during IC increased for all the neutralized HMS-containing samples relative to the non-neutralized samples, signifying that neutralization prior to IC analysis further facilitates HMS decomposition (Figure S4). The mixture with 50% HMS and 50% sulfate had an

IC yield consistent with sulfate alone, indicating complete decomposition of HMS followed by conversion of S(IV) to sulfate (Figure S4).

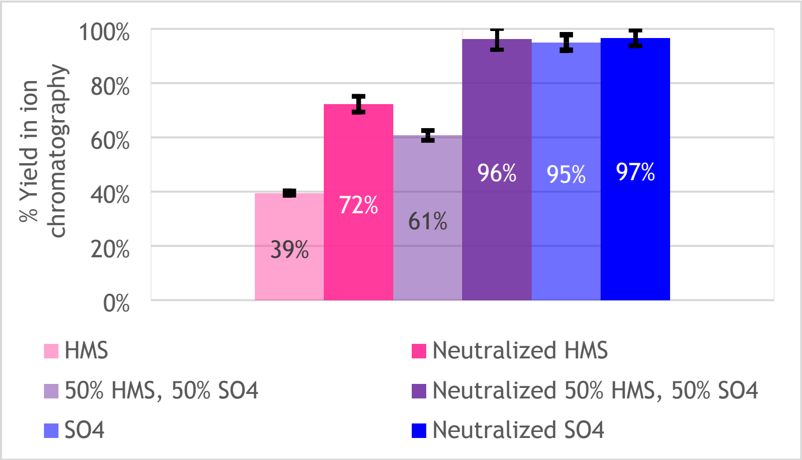

**Figure S4.** Average percent yield of sulfate measured via ion chromatography with two sample treatments: one where solutions (100% HMS, 50% HMS and 50% $SO_4^{2-}$ , and 100% $SO_4^{2-}$ ) are prepared and then measured on the IC and the other where solutions are prepared and the sample is converted to sodium form before being measured on the IC. The error bars are the standard deviation of the percent yield from 3 measurements for each experimental treatment.

Non-HMS S(IV) species ($HSO_3^-$ and $SO_3^{2-}$) are converted to sulfate when dissolved in water and oxidized by $H_2O_2$. Laboratory tests with synthetic mixtures of HMS and S(IV) confirm that both of these species are converted to sulfate during sample processing. Thus, the isotopic composition of the sulfate measured is the isotopic composition of the combined sulfate, HMS, and non-HMS

S(IV) in each sample. To obtain the isotopic composition of sulfate in the samples apart from HMS and S(IV), we corrected the isotope measurements using the measured fraction of HMS and non-HMS S(IV) species relative to sulfate as described below. Sulfate formed from HMS decomposition and S(IV) oxidation has $\Delta^{17}O = 0‰$ because the oxygen atoms of sulfite and bisulfite exchange with water and a fourth oxygen atom is added from the oxidation of S(IV) to sulfate after adding synthetic $H_2O_2$ (i.e., not formed in the atmosphere) to solution.[12] $\Delta^{17}O$ measurements were corrected by dividing the measured $\Delta^{17}O$ value by the fraction of sulfate in each sample, which were measured at Georgia Tech and described in section 1.2 (equations S6 and S7).

$$\Delta^{17}O(SO_4^{2-})_{measured} = f_{SO4} \cdot \Delta^{17}O_{SO4} + f_{S(IV)} \cdot \Delta^{17}O_{S(IV)} + f_{HMS} \cdot \Delta^{17}O_{HMS} \quad (6)$$

$$\text{where } \Delta^{17}O_{S(IV)} = \Delta^{17}O_{HMS} = 0 \text{ and } f_{SO4} + f_{S(IV)} + f_{HMS} = 1$$

$$\Delta^{17}O(SO_4^{2-}) = \Delta^{17}O(SO_4^{2-})_{measured} / f_{SO4} \quad (7)$$

The $\delta^{18}O$ of non-HMS S(IV) from the Fairbanks filter samples undergoes oxygen isotopic exchange with lab water after dissolution and during sample processing. This means that its oxygen isotopic composition will be independent of the source of S(IV) and instead is determined by the oxygen isotopic composition of lab water and the oxidants present during sample processing. Laboratory tests using dissolved reagent grade $Na_2SO_3$ and subjecting it to full sample processing yielded $\delta^{18}O$ = -1.1± 0.2‰ (n = 3). This value is used in equation 8 to correct the $\delta^{18}O$ measurements.

In non-acidic conditions, HMS decomposes in an equilibrium reaction into HCHO and $(H)SO_3^-$ (scheme 1 in Figure S3).[13] The $HSO_3^-$ then equilibrates with the laboratory water, and the $\delta^{18}O$ of the resulting sulfate depends on whether the $HSO_3^-$ is oxidized by $H_2O_2$ or $O_2$. Full-process treatment of HMS yielded $\delta^{18}O$ = 4.1 ± 2.0‰ (n = 4), indicating that the sulfate that results from decomposed HMS is more enriched than non-HMS S(IV) during the sample preparation process. We hypothesize that S(IV) resulting from HMS decomposition after the $H_2O_2$ oxidation step (e.g., during IC separation) is oxidized by isotopically heavy atmospheric molecular oxygen catalyzed by trace metals in the samples. Thus, this more enriched value is used to correct the $\delta^{18}O$ measurements in equation 8.

We prepared full-process standards with ratios of HMS, S(IV), and $SO_4^{2-}$ similar to our observations in Fairbanks (Figure S5). The measured $\delta^{18}O$ and $\Delta^{17}O$ of these mixtures are linearly proportional and reflect the amount of HMS and S(IV) in the sample ($r^2$ = 0.9968). This is consistent with the mechanism shown in Figure S3 and the experiment shown in Figure S4 where it was determined that HMS undergoes total decomposition during the sample preparation process.

Most importantly, the relationship between $\delta^{18}O$ and $\Delta^{17}O$ is linear regardless of the amount of S(IV) and HMS within the mixture. This suggests that differences in the equilibrium reaction of HMS due to varying concentrations does not elicit a detectable effect on $\delta^{18}O$ and $\Delta^{17}O$ composition. Equation S8 was used to correct $\delta^{18}O(SO_4^{2-})_{measured}$ values for S(IV) and HMS to yield the $\delta^{18}O$ of sulfate $\delta^{18}O(SO_4^{2-})$ (equation S9).

$$\delta^{18}O(SO_4^{2-})_{measured} = f_{SO4} \cdot \delta^{18}O_{SO4} + f_{S(IV)} \cdot \delta^{18}O_{S(IV)} + f_{HMS} \cdot \delta^{18}O_{HMS} \quad \textbf{(8)}$$

where $\delta\,^{18}O_{S(IV)} = -1.1‰$ and $\delta\,^{18}O_{HMS} = 4.1‰$

$$\delta^{18}O(SO_4^{2-}) = \delta^{18}O(SO_4^{2-})_{measured} / f_{SO4} \quad \textbf{(9)}$$

The total fraction of S(IV) and HMS in the samples collected in Fairbanks ranged from 0-17% and 0-20%, respectively, for $PM_{0.7}$ particles and 7-34% and 4-27%, respectively, for $PM_{>0.7}$ particles. The maximum fraction of HMS + S(IV) occurred during the highly polluted period from Jan 31st - Feb 3rd. Fractions outside of the polluted period ranged from 0-10% for S(IV) and 0-11% for HMS for $PM_{0.7}$ particles and 7-34% for S(IV) and 0-20% for HMS for $PM_{>0.7}$ particles. During the polluted period the $\delta^{18}O$ correction for combined S(IV) and HMS ranged between -0.54 and 0.81‰. For the rest of the campaign the correction for combined S(IV) and HMS ranged between -0.7 and 0.6‰. The $\delta^{18}O$ corrections for S(IV) and HMS throughout the campaign are smaller than our propagated error in $\delta^{18}O$ (±1.9‰).

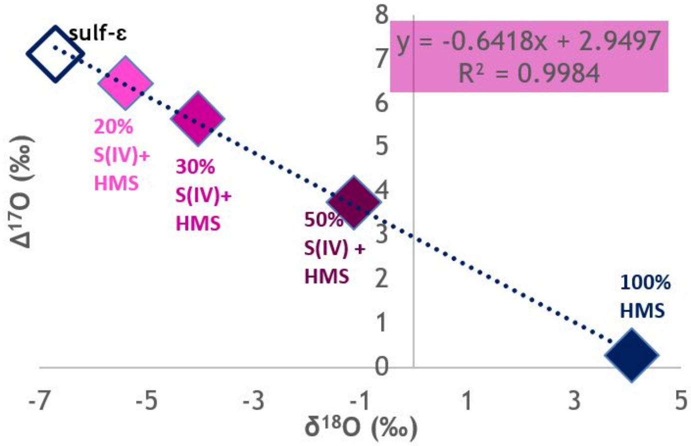

**Figure S5.** Measured $\Delta^{17}O$ and $\delta^{18}O$ of different mixtures of sulfate (sulf-e standard) and equal amounts of HMS and S(IV). The oxygen isotopic composition of sulf-e is shown in Table S3. All four mixtures were treated with the full sample preparation process (converted to sodium-form, treated twice with H2O2, and measured via IC) before the isotopic composition was measured. The molar fractions in the standards prepared are as follows:

(1) Sulf-e = 100% sulf-e;

(2) 20% S(IV) + HMS = 10% S(IV) + 10% HMS + 80% sulf-e;

(3) 30% S(IV) + HMS = 15% S(IV) + 15% HMS + 70% sulf-e;

(4) 50% S(IV) + HMS = 25% S(IV) + 25% HMS + 50% sulf-e;

(5) 100% HMS

### 1. 4.2 HMS and non-HMS S(IV) correction for sulfur isotopes

We assume negligible isotopic fractionation during high-temperature combustion of fuel oil so that $\delta^{34}S(SO_2)$ and $\delta^{34}S$ of primary sulfate are equal to our direct measurements of fuel oil (+4.7±0.6‰). Potential fractionation of $\delta^{34}S$ during the conversion of $HSO_3^-$ and $SO_3^{2-}$ to HMS is unknown. Figure S6 shows $\delta^{34}S$ values of sulfate prior to being corrected for the fraction of non-HMS S(IV) and HMS in each sample. $\delta^{34}S$ of $PM_{0.7}$ during the polluted period between January 30th and February 3rd (where the temperature ranged between -25 to -30 ˚C) increases as the fractions of HMS and non-HMS S(IV) both increase. Figures S7(a-b) and S8 show that when the fraction of HMS + S(IV) is the highest, $\delta^{34}S$ is the most enriched. Moreover, the slope, intercept, and $r^2$ of the $PM_{0.7}$ regression in Figure S7(a) is consistent with the regression with $PM_{0.7}$, $PM_{0.7-2.5}$, and $PM_{2.5-10}$ $\delta^{34}S$ in Figure S7(b). Since these size bins have very different fractions of secondary sulfate, this consistency shows that the degree of $\delta^{34}S$ enrichment is related the fraction of non-HMS S(IV) and HMS within each sample.

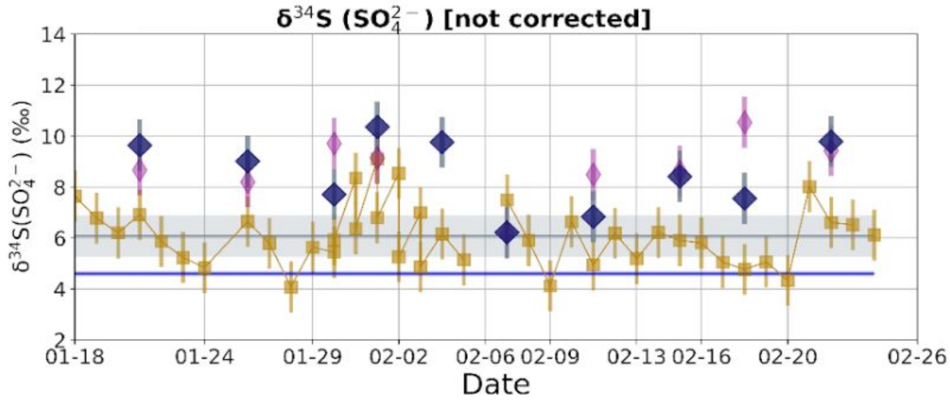

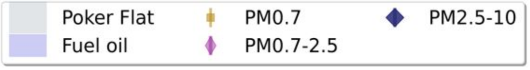

**Figure S6.** Time series of δ$^{34}$S that is not corrected for HMS+ non-HMS S(IV). Measurements are divided into three size bins: PM$_{0.7}$ (<0.7 μm) as squares, PM$_{2.5}$ (0.7-2.5 μm) as narrow diamonds, and (PM$_{2.5\text{-}10}$) (>2.5 μm) as wide diamonds. Daily PM$_{0.7\text{-}2.5}$ and PM$_{2.5\text{-}10}$ samples were combined into 10 periods as indicated by the vertical gridlines. A 2-week average of isotopic composition at Poker Flat is shown by the gray shading in a–c. The measured δ$^{34}$S source signature for Fairbanks fuel oil is shown by the blue line in c.

According to the principles of Rayleigh distillation, both lower temperatures and lower sulfur oxidation ratios will lead to larger δ$^{34}$S fractionation.[14] Both of these factors could theoretically lead to enrichment in δ$^{34}$S due to secondary oxidation being more pronounced during the polluted period, though it is also possible that the formation of sulfate from non-HMS S(IV) or HMS are responsible for this enrichment. δ$^{18}$O of PM$_{0.7}$ samples during the polluted period shows a very small contribution from secondary sulfate (11-33%), as evidenced by the high δ$^{18}$O observations (16.2±3.1‰) and model predictions detailed in section II.2 (Figure 1 in the main text). Simultaneously, Δ$^{17}$O values are at their lowest for the PM$_{0.7}$ size bin during this period (Figure S8), signifying secondary sulfate formation from O$_3$ and H$_2$O$_2$ oxidation (oxidants known to induce the largest enrichment in sulfur isotopes) are unlikely to explain the large $\delta^{34}S$ enrichment during the polluted period. This is reinforced by considering that the sulfur oxidation ratios are comparable to other periods during the campaign (Figure 1 in the main text) so fractionation due to varying SOR is unlikely to explain the $\delta^{34}S$ enrichment. Given the large contributions of non-HMS S(IV) and HMS and the small proportion of secondary sulfate during the polluted period, it is likely that the observed $\delta^{34}S$ enrichment is due to the sulfate formed from HMS and/or non-HMS S(IV) during sample processing. The fraction of HMS + non-HMS S(IV) to total sulfur species plotted in figure S7 is calculated using equation S10:

$$\text{Fraction non - HMS S(IV)} + \text{HMS} = \frac{[\text{HMS}] + [\text{non - HMS(IV)}]}{[\text{HMS}] + [\text{S(IV)}] + [\text{SO}_4^{2-}]} \quad \mathbf{(10)}$$

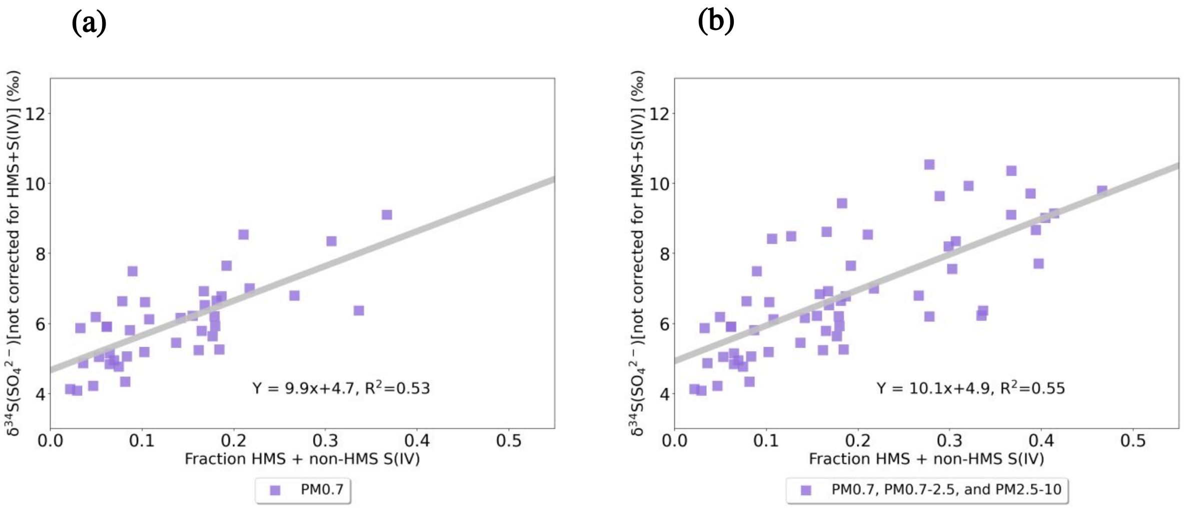

**Figure S7.** The relationship between the fraction of S(IV)+HMS in **(a)** PM$_{0.7}$and **(b)** PM$_{0.7}$, PM$_{0.7-2.5}$, and PM$_{2.5-10}$ .and δ$^{34}$S observations before HMS+S(IV) correction. The fraction of HMS+non-S(IV) is calculated with the according to equation S10.

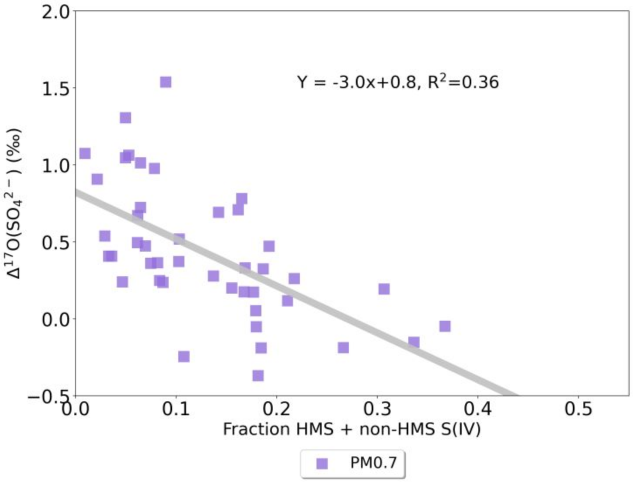

**Figure S8.** Relationship between $PM_{0.7}$ $\Delta^{17}O$ corrected for S(IV) and HMS and the fraction of S(IV) + HMS. The color bar indicates the average daily temperature in degrees Celsius. The fraction of HMS+S(IV) is calculated according to equation S10.

The difference between the modeled and observed $\delta^{34}S$ is linearly proportional to the fraction of HMS + non-HMS S(IV) ($R^2 = 0.59$, p-value <0.01) (Figure S9) The $PM_{0.7-2.5}$ and $PM_{2.5-10}$ values were not used to develop the correction equation because higher fractions of secondary sulfate in these samples make it difficult to disentangle the effects of $\delta^{34}S$ fractionation from secondary sulfate formation in the atmosphere vs. sulfate formed from HMS and non-HMS S(IV) during sample processing, though the relationship for the larger sample sizes is similar to $PM_{0.7}$.

The regression equation S11 from Figure S9 was used to determine the enrichment in $\delta^{34}S$ from decomposition of HMS and S(IV) in the samples:

$$\delta^{34}\mathrm{S}\left(\mathrm{SO}_4^{2-}\right)_{corr} = 7.3(\pm 0.60) \cdot f_{\mathrm{HMS+S(IV)}} - 1.3(\pm 0.14) \quad \textbf{(11)}$$

where $f_{HMS+S(IV)}$ is the measured fraction of HMS + S(IV) and $\delta^{34}S\left(SO_4^{2-}\right)_{corr}$ is the enrichment in $\delta^{34}S$ induced by the oxidation of S(IV) and HMS to sulfate. This assumes that the formation of sulfate from HMS and S(IV) during sample processing enriches measured $\delta^{34}S$ of sulfate relative to primary and secondary sulfate in the atmosphere. The enrichment during HMS formation alone cannot be quantitatively separated from total S(IV) as they are linearly proportional ($r^2 = 0.95$) (Figure S10). The error in the correction presented in Figure S9 was included in the fully propagated $\delta^{34}S$ error. The corrected $\delta^{34}S$ values were used as new inputs in the Bayesian mixing model to aid in estimates of the fractional contributions of different secondary sulfate formation pathways and are presented in Figures 1 and 2 of the main text.

Because total HMS and S(IV) concentrations relative to total sulfur aerosol are highest during the polluted period (11±3% and 27±6%, respectively), estimating the importance of the $NO_2$ and TMI-$O_2$ pathways based on the $\delta^{34}S$ measurements is most uncertain during this time period because the depletion in the $\delta^{34}S$ signature from these two reactions may be offset by enrichment from HMS + S(IV). This uncertainty does not substantially affect the findings of this paper as oxygen isotope measurements during the polluted period suggest that the TMI-$O_2$, $NO_2$, or OH pathways are not dominant contributors to sulfate composition (see section SII.2).

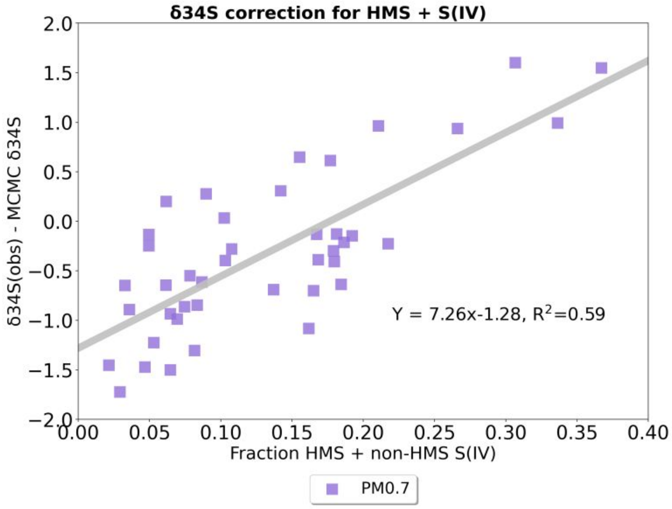

**Figure S9.** The difference between δ$^{34}$S(observations) and the MCMC δ$^{34}$S that was computed using the oxygen isotope observations, the average daily temperature, and the SOR versus the fraction of HMS + S(IV).

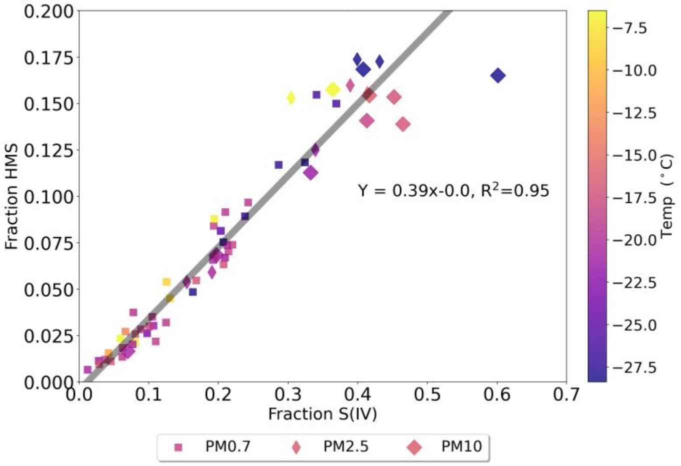

**Figure S10.** Relationship between the fraction of HMS and total S(IV) within each sample. The color bar shows the mean daily temperature during each sample collection in degrees Celsius.

## 2. Isotope observations during ALPACA

One challenge in using $\delta^{34}S(SO_4^{2-})$ to understand the sources and formation of atmospheric sulfate is that the fractionation due to secondary sulfate formation depends on the $\delta^{34}S(SO_2)$ signature, which may come from more than one source. While the measured $\delta^{34}S_{\text{fuel oil}}$ is a useful source signature of primary sulfate and fuel oil-derived $SO_2$, it's possible that enhanced vertical mixing, which is typically associated with warmer surface temperatures, may introduce coal-derived $SO_2$ to the surface. Furthermore, warmer temperatures reduce the need of fuel oil for home heating, so the relative ratios of the $\delta^{34}S(SO_2)$ signatures for fuel oil and coal may cause the source signature for coal to be important.

Figure S11 shows that there is no relationship between $\delta^{34}S$ and temperature, which indicates that coal-derived $SO_2$ does not induce a detectable effect in $\delta^{34}S$ composition, or that coal-derived $SO_2$ has a $\delta^{34}S$ value similar to fuel oil. If the $\delta^{34}S_{\text{emission}}$ signature is a mixture between coal and fuel oil-derived $SO_{2,}$ it would be most obvious during warmer periods when fuel oil consumption is lower and vertical mixing is higher.

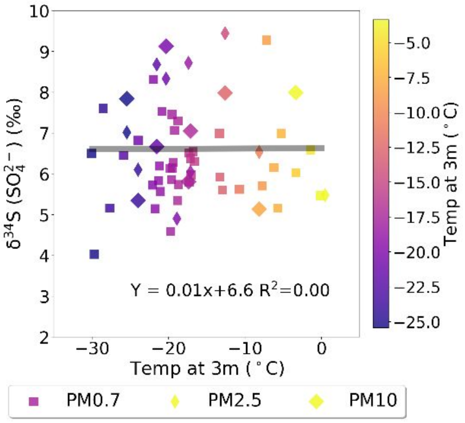

**Figure S11.** Relationship between $\delta^{34}S(SO_4^{2-})$ observations and temperature at 3m altitude in degrees Celsius.

Figure S12 shows that $SO_2$ and $SO_4^{2-}$ concentrations are lower at temperatures >-18C. The difference in $SO_2$ and $SO_4^{2-}$ concentrations during warmer periods is not reflected in the $\delta^{34}S(SO_4^{2})$ observations (Figure S11), signifying either that the sulfur isotope composition of coal-derived $SO_2$ is similar to fuel oil or that coal-derived $SO_2$ is not an important sulfur source at 3m.

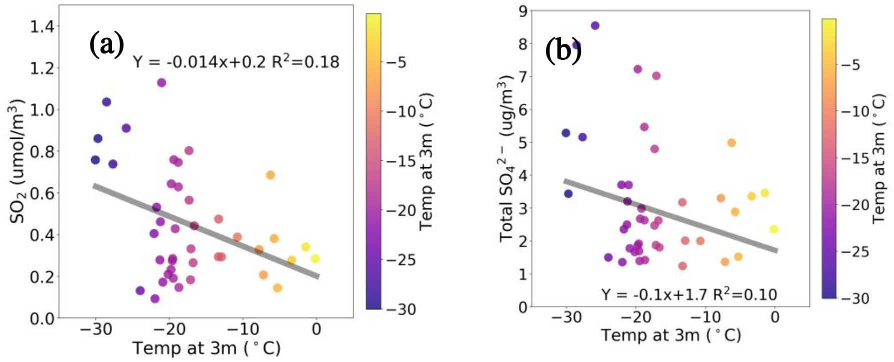

**Figure S12.** $SO_2$ **(a)** and $SO_4^{2-}$ **(b)** observations versus temperature at 3m in degrees Celsius.

Figure S13 shows a positive relationship between $SO_2$ and $SO_4^{2-}$ and no relationship between $SO_4^{2-}$ and SOR. This is consistent with a regime dominated by primary sulfate, where sulfate concentrations are largely dependent on total emissions rather than atmospheric-chemistry driven oxidation of atmospheric $SO_2$.

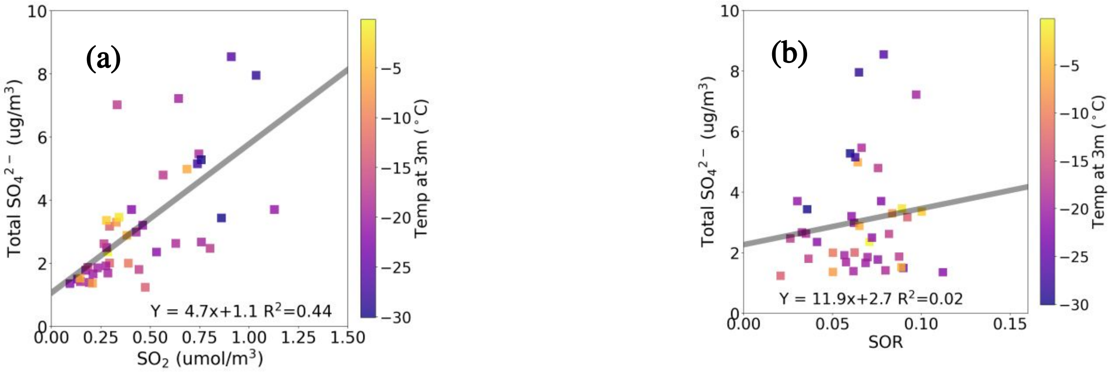

**Figure S13.** Relationship between observed $SO_4^{2-}$ and $SO_2$ **(a)** and SOR **(b)**, where SOR is defined in equation 1 in the main text.

## 3. Bayesian Isotope Mixing Model Methods and Performance

### 3.1.1 $\delta^{18}O(H_2O_{(precip)})$ and $\delta^{18}O(H_2O_{(l)})$ estimates for Fairbanks

The $\delta^{18}O$ of Fairbanks snow $\delta^{18}O(H_2O_{(precip)})$ was measured throughout the campaign with an average value of -24.8‰ (Table S5).

**Table S5.** $\delta^{18}O$ measurements (‰) from Fairbanks snow samples and laboratory water.

| Sample ID | $\delta^{18}O_{VSMOW}$ (‰) | $\delta^{18}O_{error}$ (‰) |
|---|---|---|
| CTC_ 220127 snow | -21.9 | 0.026 |
| CTC_220127_snow | -21.65 | 0.011 |
| CTC_220130_snow | -22.87 | 0.017 |
| CTC_220131_snow | -26.16 | 0.016 |
| CTC_220202_snow | -27.63 | 0.018 |
| CTC_220204_snow | -23.63 | 0.025 |
| CTC_220207_snow | -23.12 | 0.007 |
| CTC_220209_snow | -26.66 | 0.018 |
| CTC_220211_snow | -27.22 | 0.013 |
| CTC_220214_snow | -24.28 | 0.021 |
| isolab_a | -10.35 | 0.028 |
| isolab_b | -10.29 | 0.022 |
| isolab_c | -10.28 | 0.021 |
| alexanderlab_a | -10.21 | 0.022 |
| alexanderlab_b | -10.18 | 0.012 |
| alexanderlab_c | -10.18 | 0.019 |
| Average $\delta^{18}O$ Water Fairbanks | -24.767 | 0.018 |
| Average $\delta^{18}O$ Water Lab | -10.248 | 0.021 |

A regression between the $\delta^{18}O(H_2O_{(precip)})$ observations in Table S5 and the average daily ambient temperature at 3 m altitude yielded an $r^2$ of (0.60) (Figure S14(a)). These observations were compared with historical precipitation data sourced from the IAEA Water Isotope system from Alaska and Western Canada between 1953-2023. The relationship between $\delta^{18}O(H_2O_{(precip)})$ and ambient temperature in this study is consistent with historical data for this region (Figure S14b)).

The regression equation from Figure S14(b):

$$\delta^{18}O(H_2O_{(precip)}) = 0.43 \cdot T - 17.22 \quad \textbf{(12)}$$

where *T* is temperature in degrees Celsius was used to calculate $\delta^{18}O(H_2O_{(precip)})$ as a function of daily mean ambient temperature during filter sample collection. Equation 12 represents a source of uncertainty in calculating the source signatures of $\delta^{18}O$ oxidation, as the relationship between $\delta^{18}O(H_2O_{(precip)})$ and temperature was not directly measured for each sulfate sample. For a given temperature, the error in $\delta^{18}O(H_2O_{(precip)})$ is ±0.35‰, which is the error in the intercept of Figure S14(b).

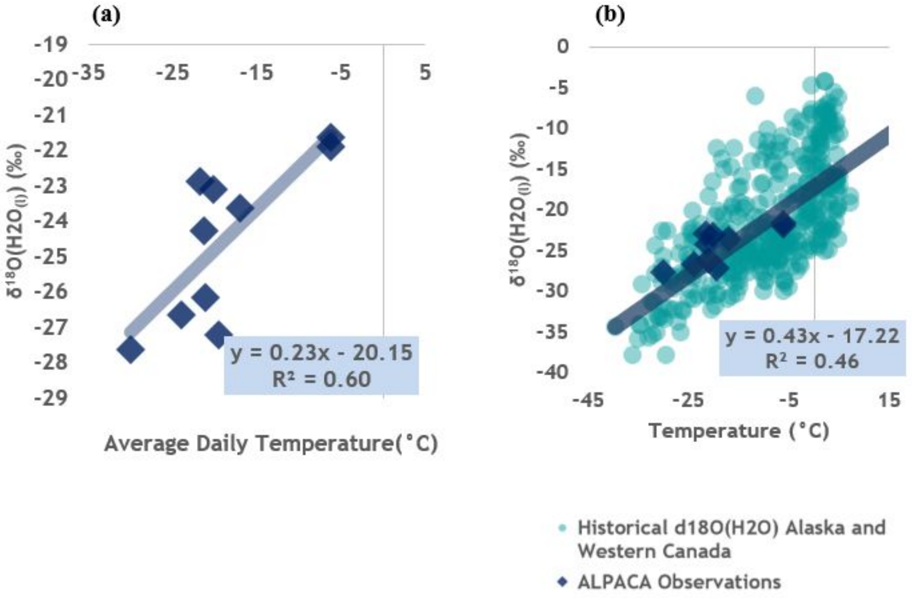

**Figure S14. (a)** $\delta^{18}O(H_2O_{(precip)})$ observations from Table S5 vs. the mean ambient temperature during sample collection in Fairbanks. The error bars for the $\delta^{18}O(H_2O_{(precip)})$ observations are smaller than the data points but are shown in Table S5. **(b)** $\delta^{18}O(H_2O_{(precip)})$ observations from Table S5 vs. the mean ambient temperature during sample collection plotted with historical precipitation data compiled from the IAEA water isotope system database from 1953-2023 from the Global Network of Isotopes in Precipitation (GNIP) Database accessible at: https://nucleus.iaea.org/wiser

Dissolved $SO_2$ equilibrates with liquid water so that the $\delta^{18}O(S(IV))$ signature is linearly dependent on the $\delta^{18}O$ of the solvent water ($r^2 = 0.992$) and more enriched by 7.8‰ on average (equation S13 from Figure S15).

$$\delta^{18}O(S(IV)) = 0.95 \cdot \delta^{18}O(H_2O_{(l)}) + 7.8 \qquad \textbf{(13)}$$

Equation S13 was determined by using the observed relationship between $\delta^{18}O(H_2O_{(l)})$ and $\delta^{18}O(SO_4^{2-})$ in laboratory experiments from Holt et al (1981) and correcting for the addition of one oxygen atom from molecular oxygen during metal-catalyzed oxidation of S(IV) to sulfate. For each sample in Fairbanks, equation S12 was used first to estimate the $\delta^{18}O(H_2O_{(precip)})$ as a function of average temperature during sample collection, and equation S13 was used to calculate the equilibrated $\delta^{18}O(S(IV))$, assuming that the $\delta^{18}O(H_2O_{(precip)})$ is equal to the $\delta^{18}O(H_2O_{(l)})$ of aerosol water. This represents a source of uncertainty because the $\delta^{18}O(H_2O_{(l)})$ of aerosol water is unknown.

We dissolved reagent sodium sulfite ($Na_2SO_3$) in laboratory Milli-Q water ($\delta^{18}O(H_2O_{(l)})$= -10.25‰ in Table S5) and measured the $\delta^{18}O(S(IV))$ composition as described in section 1.4 but without adding $H_2O_2$. The resulting $\delta^{18}O(S(IV))$ was -2.4‰. This is within analytical error (±0.8‰) of the expected $\delta^{18}O(S(IV))$ value calculated from equation S13 (-1.9‰). Additionally, we hypothesized that the measured enrichment in $\delta^{18}O(HMS)$ (+4.1‰) was from metal-catalyzed oxidation of S(IV) via $O_2$ during sample processing (section I.4). Using the $\delta^{18}O(S(IV))$ value from equation S13 and the δ$^{18}$O of molecular oxygen yielded 4.1‰ for δ$^{18}$O(HMS), which is the same as the measured value.

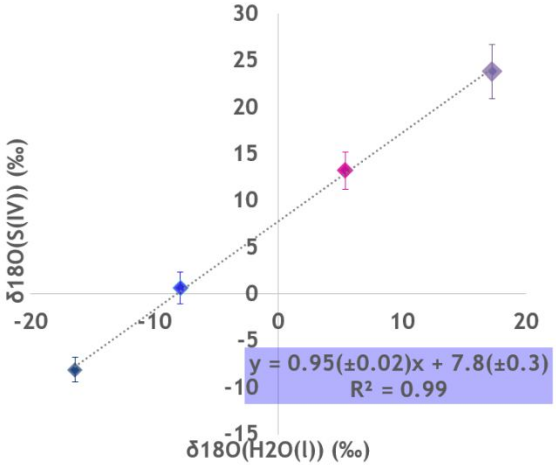

**Figure S15.** δ$^{18}$O(S(IV) as a function of the δ$^{18}$O of the solvent water (d18O(H2O(l)) from Holt (1981). Values for δ$^{18}$O(S(IV)) are corrected values of measured δ$^{18}$O($SO_4^{2-}$) from Holt 1981, accounting for the oxidation of S(IV) to sulfate from metal-catalyzed oxidation by $O_2$ in their experiments.

### 3.2 δ$^{18}$O($H_2O_{(gas)}$) estimates for Fairbanks

The isotopic exchange of $SO_2$ with water vapor yields lighter δ$^{18}$O($SO_2$) than liquid water exchange because δ$^{18}$O($H_2O_{(g)}$) is lighter than d18O(H2O(l)).[14] Bastrikov et al. (2014) measured δ$^{18}$O($H_2O_{(g)}$) continuously at the Kourovka astronomical observatory in Western Siberia (57.037°

N, 59.547° E; 300 m above sea level) ) between April 2012 and August 2013.[22] Figure S16 shows measured δ$^{18}$O($H_2O_{(g)}$) as a function of temperature at 8 meters above the surface between April 2012 and August 2013 using a Picarro L2130-I wavelength-scanned cavity ring-down spectroscopy analyzer.[15] We use the equation S14 from Figure S16 to calculate δ$^{18}$O($H_2O_{(g)}$) as a function of daily-mean temperature during the ALPACA field campaign. The δ$^{18}$O($H_2O_{(g)}$) values from Figure S16 were compared with the δ$^{18}$O($H_2O_{(l)}$) values presented in Figure S14(a-b). On average, the δ$^{18}$O($H_2O_{(g)}$) signature was -11.3‰ lighter than ($H_2O_{(l)}$), which is consistent with estimates from Broecker and Oversby (1971). Equation S15 was derived from laboratory experiments in Holt et al (1983) was used to estimate δ$^{18}$O($SO_4^{2-}$) from gas-phase oxidation by OH. The average source signatures for δ$^{18}$O($SO_4^{2-}$) used in the model are displayed in Table 1 of the main text.

$$\delta^{18}O(H_2O_{(g)}) = 0.40 \cdot T - 26.0 \qquad \textbf{(14)}$$

where $T$ is in degrees Celsius

$$\delta^{18}O\left(SO_4^{2-}\right) = 0.71 \cdot \delta^{18}\mathrm{O}(\mathrm{H_2O_{(g)}}) \qquad \textbf{(15)}$$

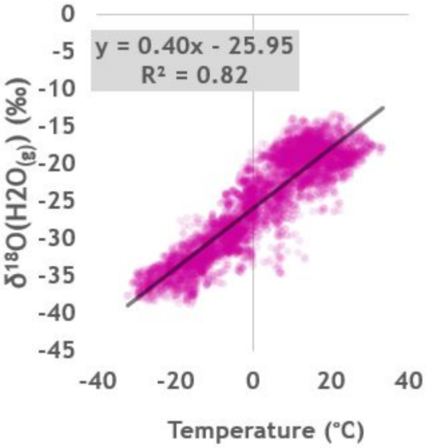

**Figure S16.** $\delta^{18}O(H_2O_{(g)})$ observations (2012-2013) vs. ambient temperature from Bastrikov et al. (2014).

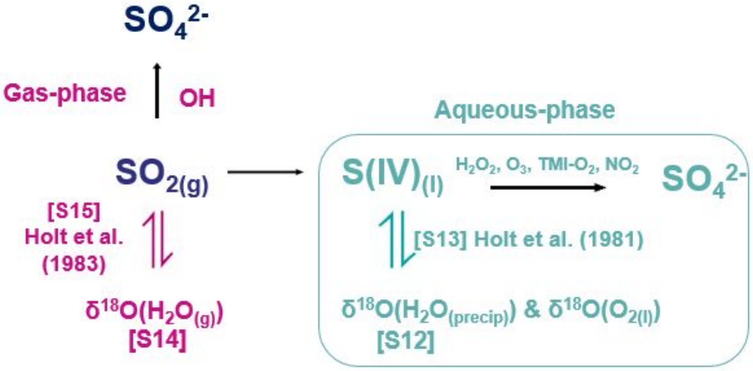

**Figure S17.** Schematic representation of the gas-phase (pink) and aqueous-phase (blue) equilibration of S(IV). $\delta^{18}O(H_2O_{(precip)})$ varies as a function of ambient temperature (equation S12). Dissolved $SO_2$ equilibrates with liquid water (equation S13), yielding a heavier $\delta^{18}O$(S(IV) signature than $\delta^{18}O(H_2O_{(l)})$. The $\delta^{18}O(H_2O_{(g)})$ values also vary as a function of temperature (equation S14), yielding a lighter $\delta^{18}O(H_2O_{(g)})$ signature than $\delta^{18}O(H_2O_{(l)})$. Equation S15 estimates the $\delta^{18}O(SO_4^{2-})$ signature from the oxidation of gas-phase $SO_2$ via OH using the $\delta^{18}O(H_2O_{(g)})$ values calculated with equation S14.[16]

### 3.3 Source Signatures for $\delta^{18}O(SO_4^{2-})$, $\Delta^{17}O(SO_4^{2-})$, and $\delta^{34}S(SO_4^{2-})$

$\delta^{18}O(SO_4^{2-})$ signature from aqueous-phase oxidation of atmospheric sulfate largely depends on the $\delta^{18}O(H_2O_{(l)})$ signature of the solvent water through isotopic exchange of S(IV) with water (equation S13). Sulfate formed from the $NO_2$ oxidation pathway has a light $\delta^{18}O$ signature of -17.2±1.6‰ because $NO_2SO_3$ decomposes and rapidly hydrolyzes to form $SO_4^{2-}$ and HONO.[17–19] TMI-O2-derived sulfate is slightly heavier (-5.3±1.2‰) as the fourth oxygen is from dissolved $O_2$. The TMI-$O_2$ path includes both the oxidation of inorganic S(IV) by Fe and Mn as well as by excited triplet states of brown carbon as these produce sulfate with the same O isotopic signature.[20,21] Both $H_2O_2$ and $O_3$ oxidation result in a heavier signature ($\delta^{18}O(SO_4^{2-})$ = +10.0±0.8 and +21.3±1.2‰, respectively) because the oxidants themselves have relatively heavy $\delta^{18}O$ values (+22 to +52‰ and +130‰, respectively).[22,23] For $H_2O_2$, the oxidant supplies two of the four oxygen atoms of sulfate, leaving a smaller contribution from isotopically light water.[24] The $H_2O_2$ path includes hydrogen peroxide formed in the particle phase and gas phase; however, we expect the gas-phase path to be minor during the most polluted periods because the very high $NO_x$ observed during the campaign may suppress formation of $H_2O_2(g)$.[25,26] We assume that the aqueous-phase source signatures consist of a weighted average between the equilibrated S(IV) calculated in equations 12 and 13 ($\delta^{18}O(S(IV))$ and the oxidants that are transferred to form product sulfate ($\delta^{18}O_{oxidant}$). It is unknown whether there is additional fractionation during these reactions. This represents a source of uncertainty in calculating the source signatures of the $H_2O_2$, $O_3$, TMI-$O_2$, and $NO_2$ pathways.

**Table S6.** $\delta^{18}O(SO_4^{2-})$, $\Delta^{17}O(SO_4^{2-})$, and $\delta^{34}S(SO_4^{2-})$ isotopic assumptions used) in the Bayesian isotope mixing model

| **Pathway** | **$\delta^{18}O(SO_4^{2-})$ (‰)**<br>**Average ±1σ‰** | **$\Delta^{17}O(SO_4^{2-})$ (‰)[a]** | **$\varepsilon_{oxidant}$[b]** |
|---|---|---|---|
| **Primary** | **+23.5‰** | **-0.34‰** | $\delta^{34}S(SO_4^{2})_{primary}$ = +4.7‰,<br>$\varepsilon_{primary}$=0.0 |
| **$O_3$** | $\delta^{18}O(S(IV)) \cdot 0.75 + \delta^{18}O(O_3) \cdot 0.25$<br>= **+ 21.0±2.3‰**<br>where $\delta^{18}O(S(IV))$ is calculated from equation S13 and $\delta^{18}O(O_3)$ = 130‰ from Vicars and Savarino (2014).[23] | **+9.8** ( *Vicars and Savarino 2014*)([23]) | Equation [S18] *(Harris et al. 2012 (a-c)([27])* |
| **$H_2O_2$** | $\delta^{18}O(S(IV)) \cdot 0.5 + \delta^{18}O(H_2O_2) \cdot 0.5$<br>= **+ 9.8±1.5‰**<br>where $\delta^{18}O(S(IV))$ is calculated from equation S13 and $\delta^{18}O(H_2O_2)$ = 35.4‰ from Savarino and Thiemens (1999).[22] | **+0.81** | Equation [S18] *(Harris et al. 2012 (a-c) ([27])* |

| | | | |
|---|---|---|---|
| **TMI-$O_2$** | $\delta^{18}O(S(IV)) \cdot 0.75 + \delta^{18}O(O_2) \cdot 0.25$<br>**= - 5.6±2.3‰**<br>where $\delta^{18}O(S(IV))$ is calculated from equation S13 and $\delta^{18}O(O_2)$ = 23.5‰.[28] | **-0.09** | Equation [S19] *(Harris et al. 2012 (a-c) (27)* |
| **$NO_2$** | $\delta^{18}O(S(IV)) \cdot 0.75 + \delta^{18}O(H_2O) \cdot 0.25$<br>**= - 17.6±3.1‰**<br>where $\delta^{18}O(S(IV))$ is calculated from equation S13 and $\delta^{18}O(H_2O_{(l)})$*) is calculated with equation S12.[19] | **0.0** | +1.0 *(Yang et al. 2018)(29)* |
| **OH** | $\delta^{18}O(SO_4^{2-}) = 0.71(\delta^{18}O(H_2O_{(g)})) +$ 16.5<br>**- 6.71 ±2.11‰**<br>where $\delta^{18}O(H_2O_{(g)})$ is calculated with equation S15. | **0.0** | Equation [S20] *(Harris et al. 2012 (a-c) (27)* |

[a] $\Delta^{17}O(SO_4^{2-}) = \delta^{17}O(SO_4^{2-}) - 0.52 \times \delta^{18}O(SO_4^{2-})$

[b] $\varepsilon_{oxidant}$ = sulfur isotopic fractionation factor where $\varepsilon_{oxidant} = (\alpha_{34\ oxidant} - 1) \times 1000$ and $\alpha_{34\ oxidant} = (^{34}S/^{32}S)_{products} / (^{34}S/^{32}S)_{reactants}$

$\Delta^{17}O(SO_4^{2-})$ refers to the enrichment of $\delta^{17}O(SO_4^{2-})$ relative to $\delta^{18}O(SO_4^{2-})$ ( equation 1 in the main text) and has been used in many studies to estimate the importance of the $H_2O_2$ ($\Delta^{17}O(SO_4^{2-})$ = +0.8 ‰) and $O_3$ ($\Delta^{17}O(SO_4^{2-})$ = +9.8 ‰) formation pathways in various environments.[18,19,22,30] $\Delta^{17}O$ values greater than zero originate during the formation of ozone in the atmosphere.[23] The enriched $\Delta^{17}O(SO_4^{2-})$ from $H_2O_2$ oxidation is from a minor $H_2O_2$ formation pathway involving $O_3$ ($OH + O_3 \rightarrow HO_2 + O_2$).[22,31] It has been shown that photoformation of $H_2O_2$ can also occur in particles and on snow grains in the Arctic, hereafter referred to as

$HOOH_{(pm).}$[2,32,33] Since Fairbanks is a cold, $NO_x$-rich environment, gas-phase $H_2O_2$ formation via $HO_2 + HO_2$ may be negligible because it cannot compete with $NO + HO_2$. This leaves the possibility that the majority of $H_2O_2$ may form in particles. In this case, the $\delta^{18}O(SO_4^{2-})$ and $\Delta^{17}O(SO_4^{2-})$ signatures of $HOOH_{(pm)}$-derived sulfate would be +4.1±1.5‰ and -0.17‰, respectively because the oxygen atoms of $H_2O_2$ are derived from dissolved $O_2$. Results of additional source signature calculations where all $H_2O_2$-derived sulfate is assumed to be the result of $HOOH_{(pm)}$ oxidation are shown in section 5.1 The OH and TMI-$O_2$ pathways have $\Delta^{17}O(SO_4^{2-})$ close to 0‰ (0‰ and -0.10 ‰ respectively) and the $\Delta^{17}O(SO_4^{2})$ of primary sulfate is -0.34 ‰.[28,34,35] The model incorporates mass balance equations S16 and S17, representing the $\delta^{18}O$ and $\Delta^{17}O$ observations with the known isotopic signatures for each respective oxidant (Table 1 of the main text).

$$\delta^{18}O\left(SO_4^{2-}\right) = f_{primary} \cdot \delta^{18}O_{primary} + f_{H_2O_2} \cdot \delta^{18}O_{H_2O_2} + f_{O3} \cdot \delta^{18}O_{O3} + f_{TMI-O_2} \cdot \delta^{18}O_{TMI-O_2} + f_{OH} \cdot \delta^{18}O_{OH} + f_{NO2} \cdot \delta^{18}O_{NO2} \qquad \textbf{(16)}$$

where $f_{primary} + f_{H2O2} + f_{O3} + f_{TMI\text{-}O2} + f_{OH} + f_{NO2} = 1$

$$\Delta^{17}O\left(SO_4^{2-}\right) = f_{primary} \cdot \Delta^{17}O_{primary} + f_{H_2O_2} \cdot \Delta^{17}O_{H_2O_2} + f_{O3} \cdot \Delta^{17}O_{O3} + f_{TMI-O_2} \cdot \Delta^{17}O_{TMI-O_2} + f_{OH} \cdot \Delta^{17}O_{OH} + f_{NO2} \cdot \Delta^{17}O_{NO2} \qquad \textbf{(17)}$$

where $f_{primary} + f_{H2O2} + f_{O3} + f_{TMI\text{-}O2} + f_{OH} + f_{NO2} = 1$

$\delta^{34}S(SO_4^{2-})$ measurements help determine secondary sulfate formation pathways because oxidants have different sulfur isotope fractionation factors during the oxidation of $SO_2$ to sulfate.[27] $\varepsilon_{oxidant}$ is the sulfur isotopic fractionation factor where $\varepsilon_{oxidant} = (\propto_{34oxidant} - 1) \times 1000$ and $\propto_{34\,oxidant} = (^{34}S/^{32}S)_{products} / (^{34}S/^{32}S)_{reactants}$. $\varepsilon_{oxidant}$ of $H_2O_2$, $O_3$, OH, and TMI-$O_2$ depends on ambient temperature during oxidation (equations S18-S20)[27].

$$\varepsilon_{H_2O_2\&\,O_3} - 1 = 16.51\ (\pm 0.15) - 0.085(\pm 0.4) \cdot T \text{ (18)}$$

$$\varepsilon_{TMI-O_2} - 1 = -5.039\ (\pm 0.044) - 0.237(\pm 0.004) \cdot T \text{ (19)}$$

$$\varepsilon_{OH} - 1 = 10.60\ (\pm 0.73) - 0.004(\pm 0.015) \cdot T \text{ (20)}$$

For average ambient temperature during Winter in Fairbanks, $H_2O_2$ and $O_3$ cause the greatest $\delta^{34}S(SO_4^{2-})$ fractionation ($\varepsilon_{H2O2\ \&\ O3} \approx +18‰$). Fractionation factors for OH and $NO_2$ are also positive ($\varepsilon_{OH} \approx +10.7‰$ and $\varepsilon_{NO2} \approx +1.0‰$).[29,36] Since the TMI-$O_2$ pathway is faster for lighter sulfur isotopes, it has a negative fractionation factor ($\varepsilon_{TMI\text{-}O2} \approx -1‰$).[36]. By principals of Rayleigh distillation, fractionation of sulfur isotopes is greater at low sulfur oxidation ratios.[14] During polluted periods in Fairbanks, sulfur emissions are mostly from ground sources and the sulfur isotope fractionation is at its highest due to low temperatures and sulfur oxidation ratios. This provides an ideal scenario for use of $\delta^{34}S$ measurements to differentiate sulfate formation pathways in Fairbanks. In these ways, combining $\delta^{18}O(SO_4^{2-})$, $\Delta^{17}O(SO_4^{2-})$, and $\delta^{34}S(SO_4^{2-})$ measurements provide complementary information about sources and formation of atmospheric sulfate.

Mass balance equation S21 incorporates a Rayleigh distillation model to calculate the $\delta^{34}S$ isotope fractionation factors ($\varepsilon$) for secondary sulfate as a function of the isotopic primary source signature ($\delta^{34}S_{emission}$), average ambient temperature during sample collection (equations S18-S20), and the secondary sulfur oxidation ratio ($SOR_{2nd}$) (calculated using equations S22 and S23). $\delta^{34}S_{emission}$ is assumed to be the same as primary sulfate since sulfur isotope fractionation from fuel oil combustion is expected to be minimal due to the high combustion temperature ($\delta^{34}S_{primary}$ = +4.7±0.6‰) (Tables 1 and S4). It should also be noted that the average daily temperature in Fairbanks (-30°C to 0.0°C) was at times colder than the lowest temperatures tested in laboratory experiments to estimate $\delta^{34}S$ fractionation factors (-25°C for $H_2O_2$, $O_3$, TMI-$O_2$, OH,) and -7°C for $NO_2$.[29,36] Yang et al. (2018) found that there was not a significant temperature difference for $NO_2$ fractionation at temperatures < 8°C, but this is still a source of uncertainty in estimating the fractional contribution of the $NO_2$ pathway.

$$\delta^{34}S\left(SO_4^{2-}\right) = f_{primary} \cdot \delta^{34}S_{primary} + (1 - f_{primary}) \cdot (\delta^{34}S_{emission} - (f_{H_2O_2} \cdot \varepsilon_{H_2O_2} + f_{O_3} \cdot \varepsilon_{O_3} + f_{TMI - O_2} \cdot \varepsilon_{TMI - O_2} + f_{OH} \cdot \varepsilon_{OH} + f_{NO2} \cdot \varepsilon_{NO_2})$$

$$\cdot \left( \ln(1 - SOR_{2nd}) \cdot \frac{1 - SOR_{2nd}}{SOR_{2nd}} \right) \text{ where } f_{primary} + f_{H2O2} + f_{O3} + f_{TMI\text{-}O2} + f_{OH} + f_{NO2} = 1 \tag{21}$$

$$SO_{4\,secondary}^{2-} = [SO_4^{2-}] \cdot (1 - f_{primary}) \tag{22}$$

$$SOR_{2nd} = \frac{[SO_{4\,secondary}^{2-}]}{[SO_{4\,secondary}^{2-}] + [SO_2]} \tag{23}$$

## 3.4 Model Performance

Figure S18(a-f) show model performance compared to observations for $\delta^{18}O$(a-b), $\Delta^{17}O$(c-d), and $\delta^{34}S$ (e-f). In Figure S18(a-d), the $r^2$ for $\delta^{18}O$ and $\Delta^{17}O$ observations vs. model output are 0.999 and 0.992, respectively. Noteworthy differences between $\delta^{18}O$ model output vs. observations occur between Jan.19-31, which are attributed to a slight underestimate in primary sulfate since $\Delta^{17}O$ performs well during this period, suggesting that $O_3$ oxidation is not being underestimated (Figure S18(a)). For higher $\delta^{18}O$, the model slightly underpredicts $\delta^{18}O$ and thus primary sulfate (Figure S18(b)). Noteworthy differences between $\Delta^{17}O$ model output vs. observations occur during the polluted period from Jan. 31 through February 1. This slight disagreement is not present in model output when all $H_2O_2$ is assumed to come from the particle-phase formation pathway (HOOH(pm), where $\Delta^{17}O = 0.0$ ‰) vs. $H_2O_2$ formed in the gas-phase ($\Delta^{17}O = 0.8$‰) (see section 5 of supporting information). Due to the high NOx concentrations during the polluted period, it's possible that gas-phase formation of $H_2O_2$ is not an important oxidant source for sulfate formation, which would explain the small discrepancy in the model output $\Delta^{17}O$ and observations. Regardless of the source signatures used for $H_2O_2$, the fractional contribution for $H_2O_2$ is similar in the model output so this is likely not a large source of error in estimating the fractional contribution of sulfate formed through $H_2O_2$ oxidation.

In Figure S18(e-f), the $r^2$ for $\delta^{34}S$ observations vs. MCMC output is 0.81. MCMC $\delta^{34}S$ is generally higher than the observations, though most of the 95% confidence intervals overlap with observations (noteworthy differences are Jan. 23-29, Feb. 6, and Feb. 25). For the disagreement in early January, this is likely due to an underestimate in primary sulfate shown in Figure S18(a-b). MCMC $\delta^{34}S$ is lower than $\delta^{34}S$ observations during the polluted period, particularly during the daytime on January 31st. Given the good MCMC agreement with oxygen observations these discrepancies in the $\delta^{34}S$ portion of the model is likely only a minor source of error in the final estimates for the fractional contributions of the six sulfate formation pathways.

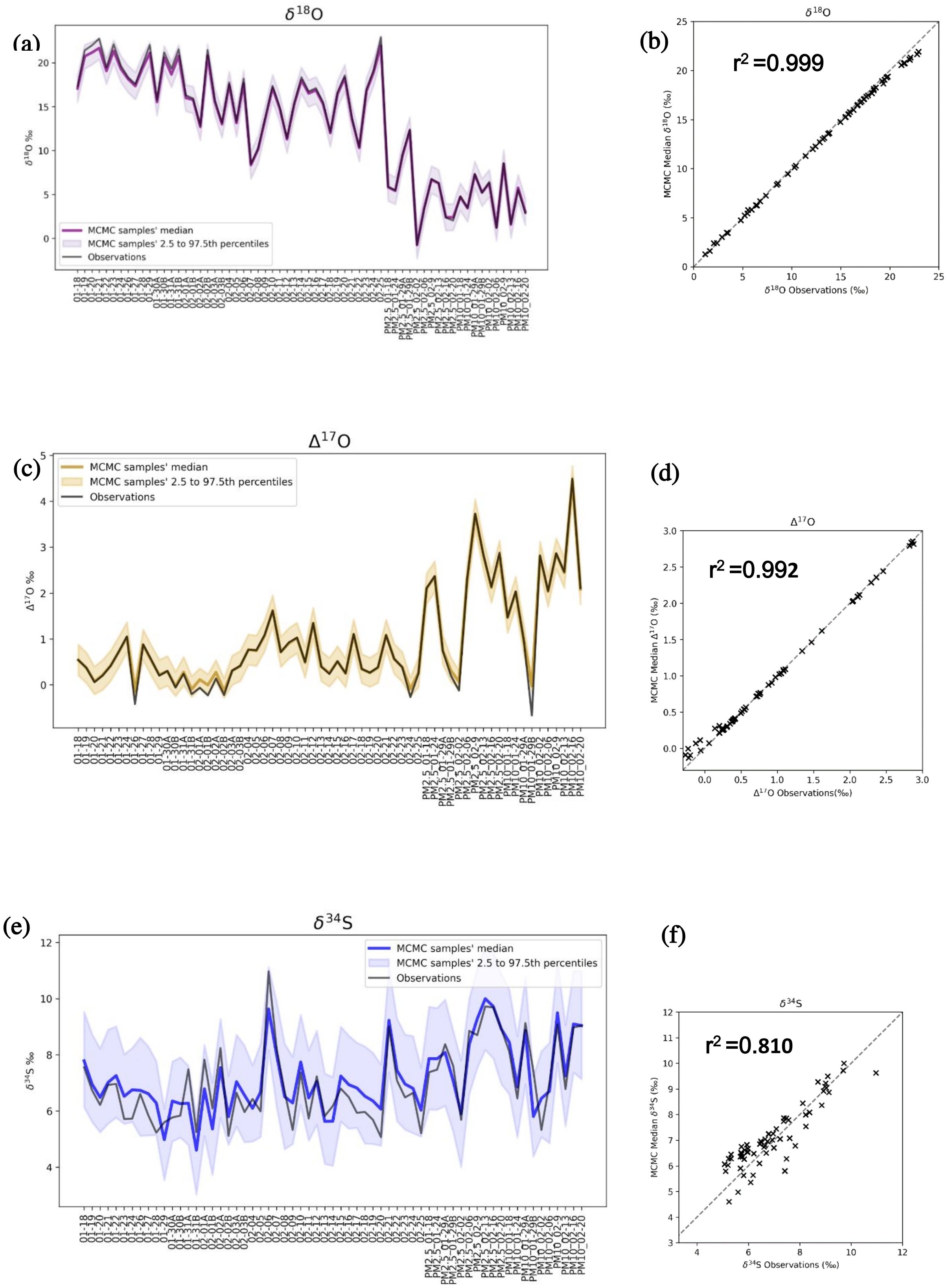
(a)
δ18O
δ18O ‰
MCMC samples' median
MCMC samples' 2.5 to 97.5th percentiles
Observations
(b)
δ18O
r2 =0.999
MCMC Median δ18O (‰)
δ18O Observations (‰)
(c)
Δ17O
Δ17O ‰
MCMC samples' median
MCMC samples' 2.5 to 97.5th percentiles
Observations
(d)
Δ17O
r2 =0.992
MCMC Median Δ17O (‰)
Δ17O Observations(‰)
(e)
δ34S
δ34S ‰
MCMC samples' median
MCMC samples' 2.5 to 97.5th percentiles
Observations
(f)
δ34S
r2 =0.810
MCMC Median δ34S (‰)
δ34S Observations (‰)

**Figure S18(a).** Calculated MCMC median (purple) and observed (black) $\delta^{18}$O values throughout the campaign. The shading represents the 95% confidence interval in the model's ability to reproduce observations. **(b) .** Linear least-squares regression of $\delta^{18}$O observations vs. MCMC output. **Figure S18(c).** Calculated MCMC median (gold) and observed (black) $\Delta^{17}$O values throughout the campaign. The shading represents the 95% confidence interval in the model's ability to reproduce observations. **(d)(.** Linear least-squares regression of $\Delta^{17}$O observations vs. MCMC output. **Figure S18(e).** Calculated MCMC median (gold) and observed (black) $\delta^{34}$S values throughout the campaign. The shading represents the 95% confidence interval in the model's ability to reproduce observations.**(f).** Linear least-squares regression of $\delta^{34}$S observations vs. MCMC output.

## 4. Bayesian Isotope Mixing Model Results

### 4. 1 Time series of fractional contributions of primary and secondary sulfate

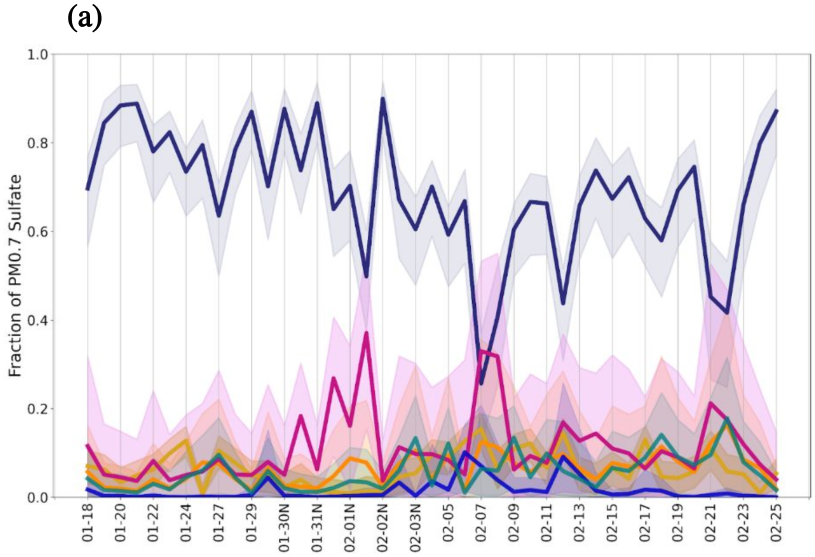

**Figure S19 (a-c).** MCMC median modeled fractions for the sources and formation pathways of Fairbanks for $PM_{0.7}$ sulfate **(a)**, $PM_{0.7\text{-}2.5}$ sulfate **(b),** and $PM_{2.5\text{-}10}$ sulfate **(c).** The shading represents the 95% confidence interval for each sulfate formation pathway.

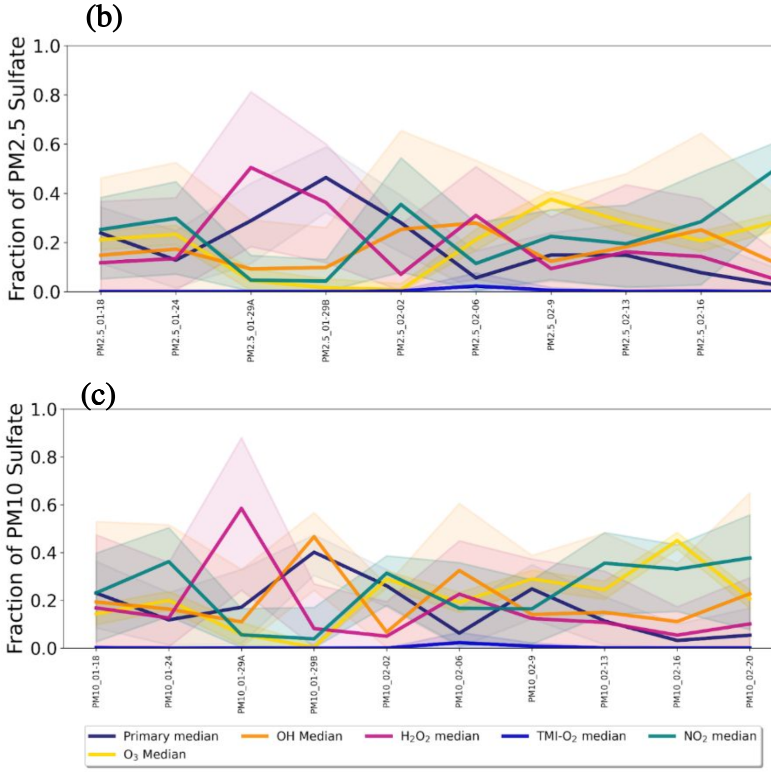

## 4. 2 Secondary Sulfate and HMS mass concentrations

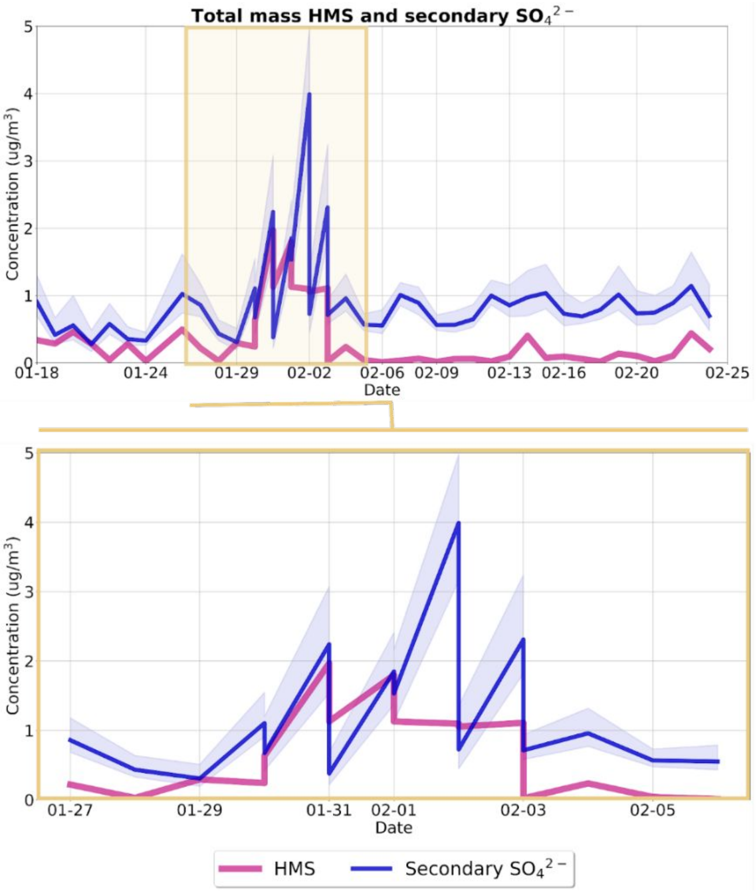

**Figure S20**. Mass concentrations of total secondary sulfate (blue) and HMS (pink) throughout the campaign. The blue shading shows the 95% confidence interval for secondary sulfate from the MCMC model.

## 4. 3 Linear regressions of secondary sulfate formation pathways

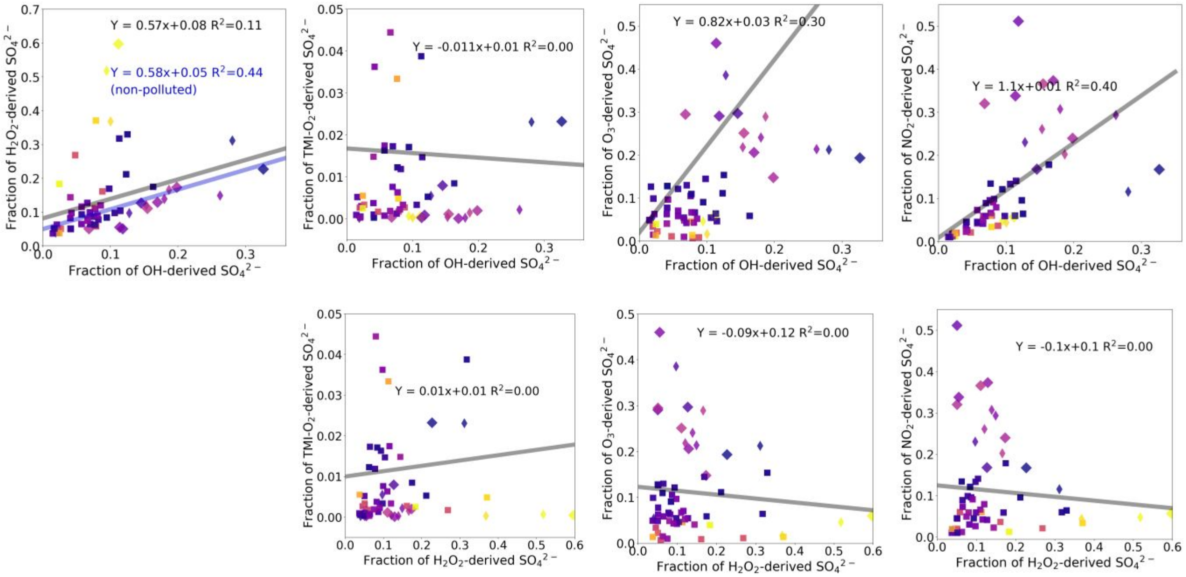

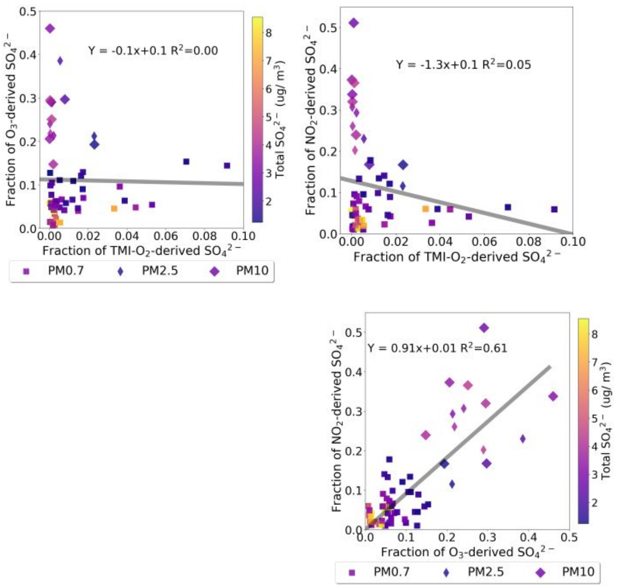

**Figure S21.** Linear regressions of secondary oxidation pathways for sulfate formation in Fairbanks.

Figure S21 shows linear regressions of secondary oxidation pathways for sulfate formation in Fairbanks. The $NO_2$ vs. OH regressions ($r^2$= 0.40, p-value <0.01) suggests association between the two photochemically-driven sulfate formation pathways. Sulfate from $O_3$ is also weakly associated with OH-derived sulfate ($r^2$= 0.30). There is no association between TMI- $O_2$ versus OH ($r^2$= 0.00), $O_3$ ($r^2$ = 0.00), or $NO_2$ ($r^2$ = 0.05), which indicates that the MCMC model can differentiate between these pathways despite their similar $\Delta^{17}O$ source signatures. $O_3$ and $NO_2$, which are both pH-sensitive sulfate formation pathways, are not associated with $H_2O_2$-derived sulfate ($r^2$= 0.00 for both). $O_3$ and $NO_2$ -derived sulfate show the strongest correlation among the secondary sulfate formation pathways ($r^2$= 0.61, p-value < 0.01), as expected due to their similar pH-dependencies.

The fraction of $O_3$-derived sulfate is moderately correlated with ambient $O_3$ concentrations with $r^2$= 0.40 for $PM_{0.7}$ and $r^2$ =0.30 for $PM_{>0.7}$ (figure S22(a-b)).

## 4. 4 Isotope mixing model results comparison with measured ambient $O_3$ and metal concentrations

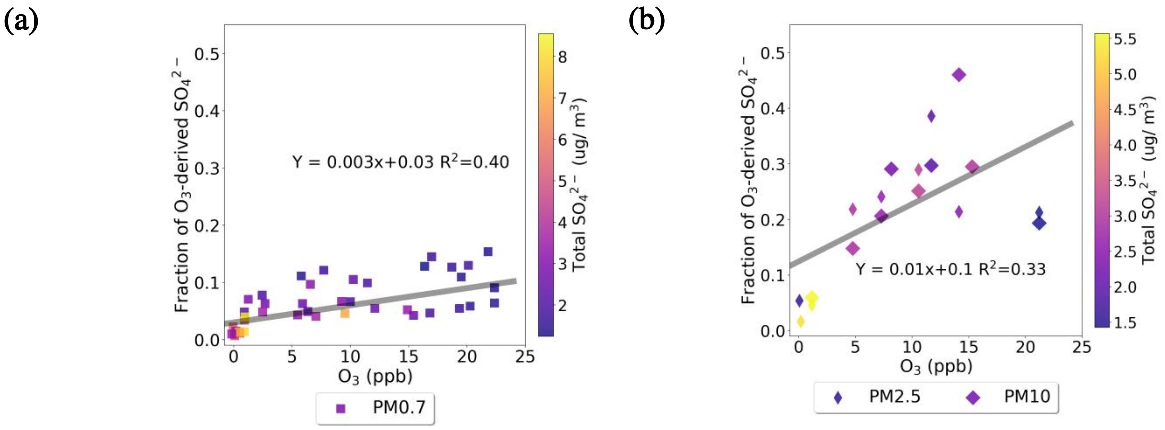

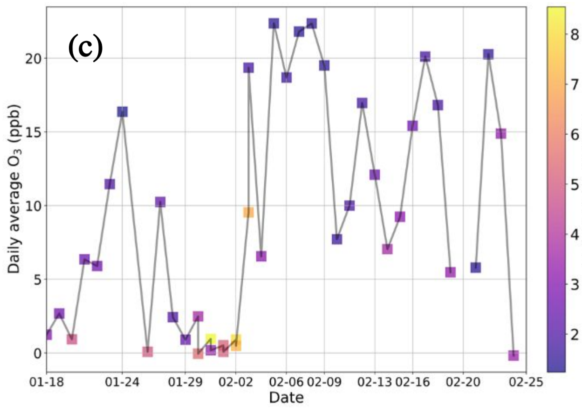

**Figure S22(a).** The relationship between the fraction of $O_3$-derived sulfate and ambient $O_3$ concentrations (ppb) for $PM_{0.7}$ particles. **(b).** The relationship between the fraction of $O_3$-derived sulfate vs. ambient $O_3$ concentrations (ppb) for $PM_{>0.7}$ particles. **(c).** Time series of ambient $O_3$ concentrations (ppb) throughout the campaign.

Water-soluble metal concentrations were measured with the same tecnique as Yang and Weber (2022).[37] Briefly, filters collected at CTC were divided and shipped to the Georgia Institute of Technology. Two 1-inch punches were taken from the filters and extracted in 12mL of 18 MΩ cm$^{-1}$ water before 30 minutes of sonication (Ultrasonic Cleanser, VWR International LLC, West Chester, PA, USA). Water-soluble metals were filtered through a 0.45 μm PTFE syringe filter (Fisherbrand™). Metals were measured using inductively coupled plasma mass spectrometry (ICP-MS, Agilent 7500a series, Agilent Technologies, Inc., CA, USA). Boxplots of bulk water-soluble manganese and iron concentrations are plotted in Figure S23.

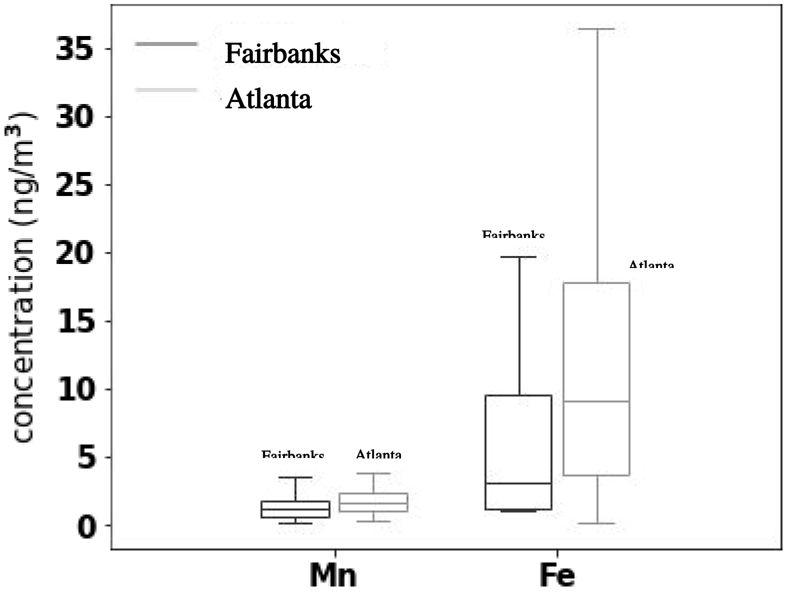

**Figure S23.** Bulk aerosol water-soluble metal concentrations in (ng/m$^3$) for Atlanta (silver) and Fairbanks (black) for manganese (left) and iron (right).

## 5. Additional Markov Chain Monte Carlo Simulations

### 5.1 Mechanisms for $H_2O_2$ formation in particles via the $HOOH_{pm}$ pathway.

In this section, we explore the assumption that all $H_2O_2$ is formed in particles via the $HOOH_{pm}$ pathway rather than via the gas-phase reaction $HO_2 + HO_2 \rightarrow H_2O_2 + O_2$.

We describe three possible reaction sequences to form HOOH(pm). In all three reaction sequences, both oxygen atoms of HOOH(pm) are derived from dissolved molecular oxygen. Sulfate that forms from oxidation by HOOH(pm) will derive two oxygen atoms from sulfite and two from dissolved oxygen (see Table S7 for MCMC assumptions).

Brown carbon-mediated formation of HOOH in particles is summarized in scheme 2 (reactions 1-5). Aromatic carbonyls (ArCHO), as representative brown carbon compounds, absorb light to form excited triplet states (scheme 2, reaction 1). The triplets are then reduced by phenols (ArOH), which are abundant in wood smoke, to form a ketyl radical (scheme 2, reaction 2). The ketyl radical reacts with $\mathrm{O_2}$ (dissolved oxygen) to form an aromatic peroxyl radical, and subsequently, aqueous $\mathrm{HOO^{\bullet}}$ and the parent ArCHO compound (scheme 2, reaction 3). This is then followed by the self-disproportionation of aqueous $\mathrm{HOO^{\bullet}}$ to form HOOH (scheme 2, reaction 4), and Cu(I)-catalyzed reduction of aqueous $\mathrm{HOO^{\bullet}}$ to HOOH (scheme2, reaction 5).

Scheme 2: Brown carbon-mediated formation of HOOH in particles from Anastasio et al., 1997[38]

$\mathrm{ArCHO} \xrightarrow{\mathrm{hv}} {}^{3*}[\mathrm{ArCHO}]$ (excited state triplet) [Scheme 2, reaction 1]

${}^{3}[\mathrm{ArCHO}]^{*} + \mathrm{ArOH} \rightarrow \mathrm{ArC^{\cdot}(H)OH} + \mathrm{ArO^{\cdot}}$ [Scheme 2, reaction 2]

$\mathrm{ArC^{\cdot}(H)OH} + \mathrm{O_2} \rightarrow \mathrm{ArC^{\cdot}(H)(OO^{\cdot})OH} \rightarrow \mathrm{ArCHO} + HOO^{\cdot}$ [Scheme 2, reaction 3]

$\mathrm{HOO^{\cdot}} + \mathrm{HOO^{\cdot}} \rightarrow \mathrm{HOOH} + \mathrm{O_2}$ [Scheme 2, reaction 4]

$\mathrm{HOO^{\cdot}} + \mathrm{Cu^{+}} \xrightarrow{\mathrm{H+}} \mathrm{HOOH} + \mathrm{O_2}$ [Scheme 2, reaction 5]

Scheme 3: ${}^{3}\mathrm{C}^{*} + \mathrm{S(IV)}$Mechanisms (Wang et al. 2020):Electron transfer to $\mathrm{T}^{*}$

$\mathrm{HSO_3^{-}} + {}^{*}\mathrm{T} \rightarrow \mathrm{HSO_3^{\cdot}} + \mathrm{T^{\cdot -}}$ [Scheme 3, reaction 1]

$\mathrm{HSO^{\cdot}_{3(aq)}} \rightarrow \mathrm{SO_3^{-}} + \mathrm{H^{+}}$ (rapid equilibrium) [Scheme 3, reaction 2]

$O_2 + SO_3^{-} \rightarrow SO_5^{-}$ [Scheme 3, reaction 3]

$SO_5^{-} + SO_5^{-} \rightarrow 2\ SO_4^{-} + O_2$ [Scheme 3, reaction 4]

$SO_4^{-} + HSO_3^{-} \rightarrow SO_3^{-} + H^{+} + SO_4^{2-}$ [Scheme 3, reaction 5]

Scheme 4: ${}^{3}C^{*} + S(IV)$ Mechanisms (Wang et al. 2020):Hydrogen transfer to $T^{*}$

$HSO_3^{-} + {}^{*}T \rightarrow SO_3^{-} + HT^{\cdot}$ [Scheme 4, reaction 1]

$SO_{3(aq)}^{-} + O_{2(aq)} \rightarrow SO_5^{-}$ [Scheme 4, reaction 2]

$SO_5^{-} + SO_5^{-} \rightarrow 2SO_4^{-} + O_2$ [Scheme 4, reaction 4]

$SO_4^{-} + HSO_3^{-} \rightarrow SO_3^{-} + H^{+} + SO_4^{2-}$ [Scheme 4, reaction 5]

**Table S7.** $\delta^{18}O(SO_4^{2-})$, $\Delta^{17}O(SO_4^{2-})$, and $\delta^{34}S(SO_4^{2-})$ isotopic assumptions used in Markov-Chain Monte Carlo (MCMC) isotope mixing model using the HOOH(pm) source signatures

| **Pathway** | **$\delta^{18}O(SO_4^{2-})$ (‰)**<br>**Average ±1σ‰** | **$\Delta^{17}O(SO_4^{2-})$ (‰)$^{a}$** | **$\varepsilon_{oxidant}{}^{b}$** |
|---|---|---|---|
| **Primary** | **+23.5‰** | **-0.34‰** | $\delta^{34}S(SO_4^{2})_{primary}$ = +4.7‰,<br>$\varepsilon_{primary}$=0.0 |
| **$O_3$** | $\delta^{18}O(S(IV))\cdot 0.75+\delta^{18}O(O_3)\cdot 0.25$<br>**= + 21.0±2.3‰**<br>where $\delta^{18}O(S(IV))$ is calculated from equation S13 and $\delta^{18}O(O_3)$ = 130‰ from Vicars and Savarino (2014).[23] | **+9.8** ( *Vicars and Savarino 2014*)(23) | Equation [S18] *(Harris et al. 2012 (a-c)*[27] |
| **HOOH(pm)** | $\delta^{18}O(S(IV))\cdot 0.5+\delta^{18}O(HOOH(pm))\cdot 0$<br>**= + 4.1 ± 1.5‰**<br>where $\delta^{18}O(S(IV))$ is calculated from equation S13 and $\delta^{18}O(HOOH(pm))$ = 23.5‰ from schemes 2-4.[22] | **-0.17** | Equation [S18] *(Harris et al. 2012 (a-c)*[27] |

| | | | |
|---|---|---|---|
| **TMI-$O_2$** | $\delta^{18}O(S(IV)) \cdot 0.75 + \delta^{18}O(O_2) \cdot 0.25$<br>**= - 5.6±2.3‰**<br>where $\delta^{18}O(S(IV))$ is calculated from equation S13 and $\delta^{18}O(O_2)$ = 23.5‰.[28] | **-0.09** | Equation [S19] *(Harris et al. 2012 (a-c)*[27] |
| **$NO_2$** | $\delta^{18}O(S(IV)) \cdot 0.75 + \delta^{18}O(H_2O) \cdot 0.25$<br>**= - 17.6±3.1‰**<br>where $\delta^{18}O(S(IV))$ is calculated from equation S13 and $\delta^{18}O(H_2O_{(l)})$*) is calculated with equation S12.[19] | **0.0** | +1.0 *(Yang et al. 2018)*[29] |
| **OH** | $0.71(\delta^{18}O(H_2O_{(g)})) + 16.5$<br>**-6.71 ±2.11‰**<br>where $\delta^{18}O(H_2O_{(g)})$ is calculated with equation S15. | **0.0** | Equation [S20] *(Harris et al. 2012 (a-c)*[27] |

[a] $\Delta^{17}O(SO_4^{2-}) = \delta^{17}O(SO_4^{2-}) - 0.52 \times \delta^{18}O(SO_4^{2-})$

[b] $\varepsilon_{oxidant}$ = sulfur isotopic fractionation factor where $\varepsilon_{oxidant} = (\alpha_{34\ oxidant} - 1) \times 1000$ and $\alpha_{34\ oxidant} = (^{34}S/^{32}S)_{products} / (^{34}S/^{32}S)_{reactants}$

### 5.2 Model performance for $HOOH_{pm}$ simulation

There is not a statistically significant difference between MCMC-estimated fractional contributions from the six sulfate formation pathways regardless of the $H_2O_2$ signature used (Tables S8 and S9). The $r^2$ of the least-squares regression comparing model output to the $\delta^{18}O(SO_4^{2-})$ observations is about the same when the HOOH(pm) signature from Table S7 is used (Figures S18(b) and S25(b)). For $\Delta^{17}O(SO_4^{2-})$, there is slightly better agreement for MCMC output and observations for the HOOH(pm) simulation ($r^2$ = 0.995, Figure S25(d)) compared to when assuming gas-phase production of $H_2O_2$ ($r^2$ = 0.991, Figure S18(d)). Due to the high NOx concentrations during the polluted period, it is likely that the gas-phase formation of $H_2O_2$ is minor, which would explain why there is slightly better agreement with $\Delta^{17}O$ model output and observations when the HOOH(pm) signature is used. Model performance for $\delta^{34}S$ is the same for both simulations, as expected given that sulfur isotope fractionation is the same regardless of whether the $H_2O_2$ is formed in the gas or particle phase.

(a)

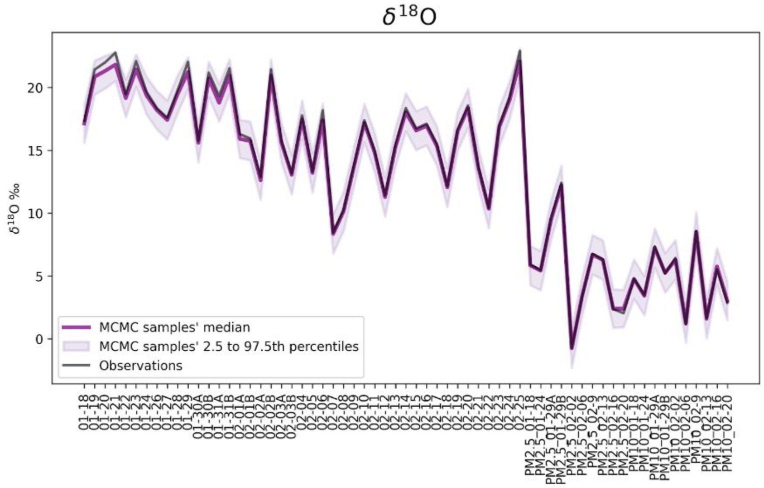

(b)

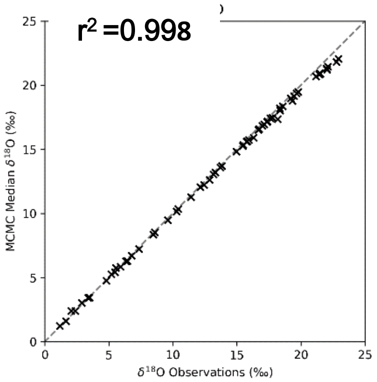

(c)

(d)

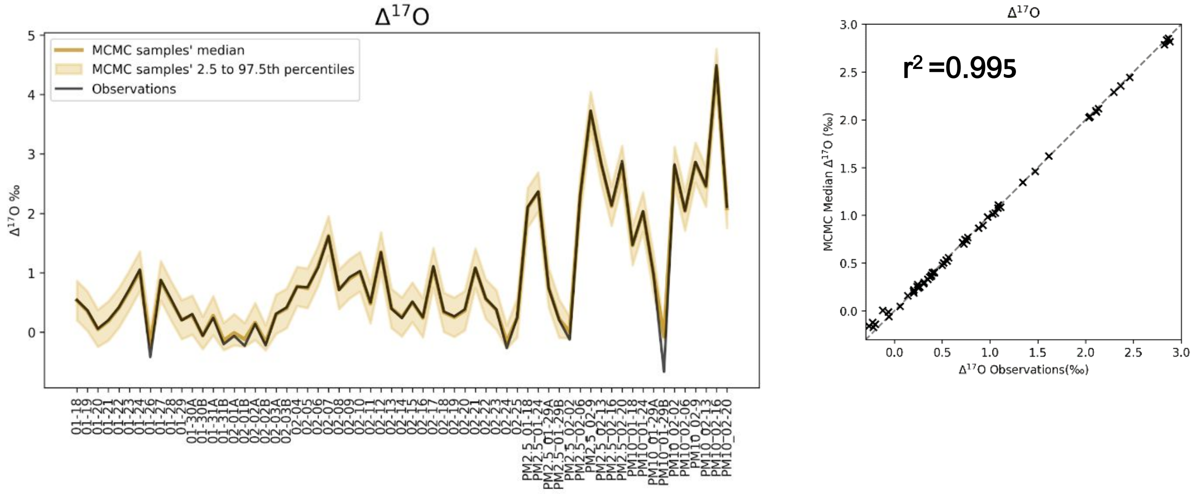

(e)

(f)

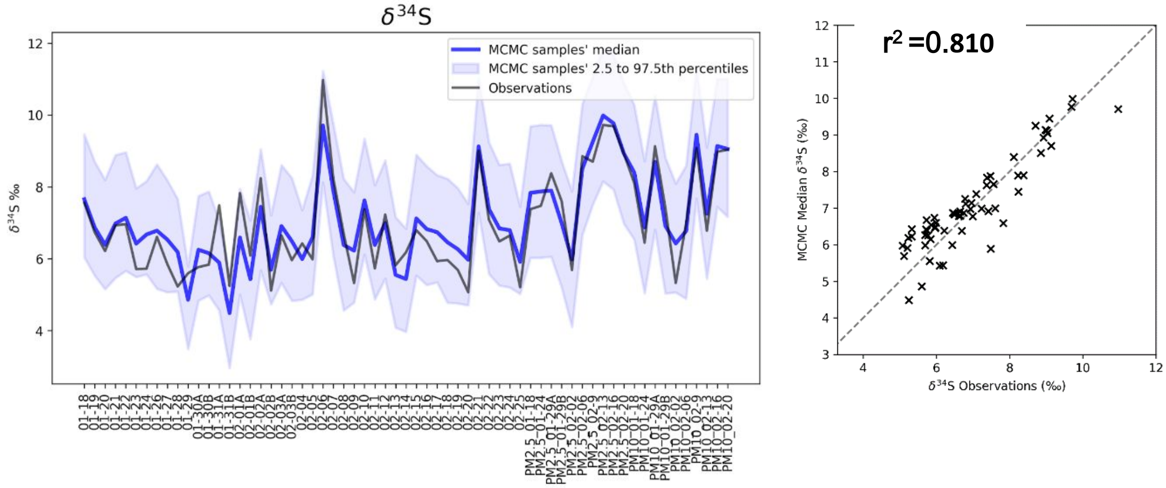

**Figure S24(a).** Calculated MCMC median (purple) and observed (black) δ$^{18}$O values throughout the campaign when all $H_2O_2$ is formed in the particle phase. The shading represents the 95%

confidence interval in the model's ability to reproduce observations. **(b).** Linear least-squares regression of $\delta^{18}O$ observations vs. MCMC output when all $H_2O_2$ is formed in the particle phase.

**(c).** Calculated MCMC median (purple) and observed (black) $\Delta^{17}O$ values throughout the campaign when all $H_2O_2$ is formed in the particle phase. The shading represents the 95% confidence interval in the model's ability to reproduce observations. **(d).** Linear least-squares regression of $\Delta^{17}O$ observations vs. MCMC output when all $H_2O_2$ is formed in the particle phase.

**(e).** Calculated MCMC median (purple) and observed (black) $\delta^{34}S$ values throughout the campaign when all $H_2O_2$ is formed in the particle phase. The shading represents the 95% confidence interval in the model's ability to reproduce observations. **(f).** Linear least-squares regression of $\delta^{34}S$ observations vs. MCMC output when all $H_2O_2$ is formed in the particle phase.

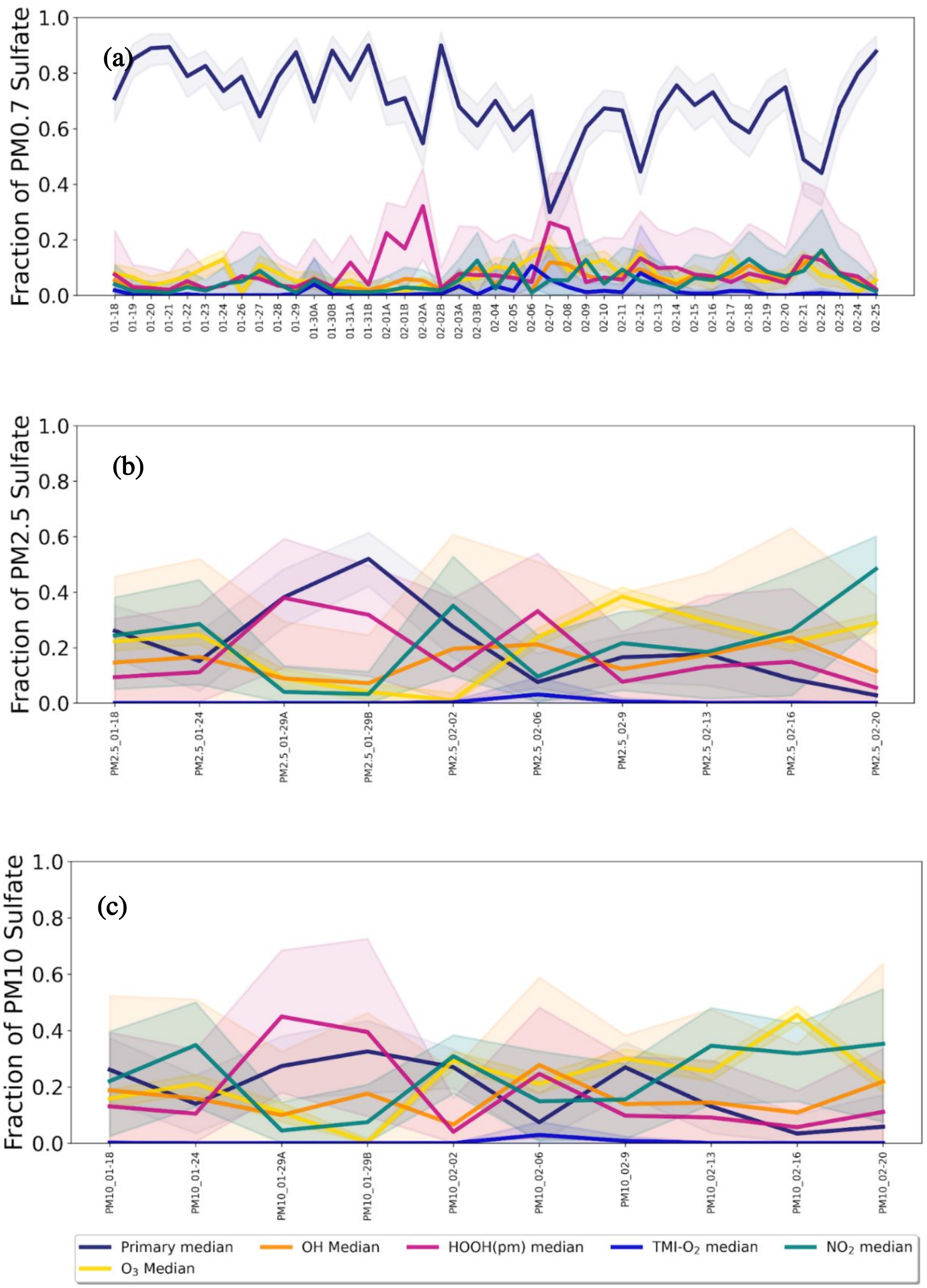

**Figure S25 (a-c).** MCMC median modeled fractions for the sources and formation pathways of Fairbanks for PM$_{0.7}$ sulfate **(a)**, PM$_{0.7\text{-}2.5}$ sulfate **(b),** and PM$_{2.5\text{-}10}$ sulfate **(c)** using source signatures from Table S7. The shading represents the 95% confidence interval for each sulfate formation pathway.

**Table S8.** Two-sample T-test for MCMC output using $H_2O_2$ or HOOH(pm) isotopic signatures for $PM_{0.7}$ sulfate

| **Statistic** | **MCMC assumption** | **Fraction primary** | **Fraction OH** | **Fraction $H_2O_2$** | **Fraction TMI-$O_2$** | **Fraction $O_3$** | **Fraction $NO_2$** |
|---|---|---|---|---|---|---|---|

| | | | | | | | |
|---|---|---|---|---|---|---|---|
| Average± Stdev | $H_2O_2$ | 69±14%<br>n=43 | 6±4%<br>n=43 | 11±8%<br>n=43 | 2±2%<br>n=43 | 6±4%<br>n=43 | 6±4%<br>n=43 |
| Average | HOOH(pm) | 70±11%<br>n=43 | 6±2%<br>n=43 | 9±5%<br>n=43 | 2±1%<br>n=43 | 7±3%<br>n=43 | 6±2%<br>n=43 |
| Significant Difference? | | no | no | no | no | no | no |
| p-value | | 0.14 | 1.00 | 0.17 | 1.00 | 0.19 | 1.00 |

**Table S9.** Two-sample T-test for MCMC output using $H_2O_2$ or HOOH(pm) isotopic signatures for $PM_{>0.7}$ sulfate

| **Statistic** | **MCMC assumption** | **Fraction primary** | **Fraction OH** | **Fraction $H_2O_2$** | **Fraction TMI-$O_2$** | **Fraction $O_3$** | **Fraction $NO_2$** |
|---|---|---|---|---|---|---|---|
| Average± Stdev | $H_2O_2$ | 18±12%<br>n=18 | 16±6%<br>n=18 | 20±15%<br>n=18 | 0±1%<br>n=18 | 22±10%<br>n=18 | 24±12%<br>n=18 |
| Average | HOOH(pm) | 21±14%<br>n=18 | 15±5%<br>n=18 | 17±12%<br>n=18 | 0±1%<br>n=18 | 24±10%<br>n=18 | 23±12%<br>n=18 |
| Significant Difference? | | no | no | no | no | no | no |
| p-value | | 0.14 | 1.00 | 0.17 | 1.00 | 0.19 | 1.00 |

## References

(1) Ma, T.; Furutani, H.; Duan, F.; Kimoto, T.; Jiang, J.; Zhang, Q.; Xu, X.; Wang, Y.; Gao, J.; Geng, G.; Li, M.; Song, S.; Ma, Y.; Che, F.; Wang, J.; Zhu, L.; Huang, T.; Toyoda, M.; He, K. Contribution of Hydroxymethanesulfonate (HMS) to Severe Winter Haze in the North China Plain. *Atmospheric Chem. Phys.* **2020**, *20* (10), 5887–5897. https://doi.org/10.5194/acp-20-5887-2020.

(2) Moch, J. M.; Dovrou, E.; Mickley, L. J.; Keutsch, F. N.; Liu, Z.; Wang, Y.; Dombek, T. L.; Kuwata, M.; Budisulistiorini, S. H.; Yang, L.; Decesari, S.; Paglione, M.; Alexander, B.; Shao, J.; Munger, J. W.; Jacob, D. J. Global Importance of Hydroxymethanesulfonate in Ambient Particulate Matter: Implications for Air Quality. *J. Geophys. Res. Atmospheres* **2020**, *125* (18). https://doi.org/10.1029/2020JD032706.

(3) Song, S.; Ma, T.; Zhang, Y.; Shen, L.; Liu, P.; Li, K.; Zhai, S.; Zheng, H.; Gao, M.; Moch, J. M.; Duan, F.; He, K.; McElroy, M. B. Global Modeling of Heterogeneous Hydroxymethanesulfonate Chemistry. *Atmospheric Chem. Phys.* **2021**, *21* (1), 457–481. https://doi.org/10.5194/acp-21-457-2021.

(4) Neubauer, K. R.; Sum, S. T.; Johnston, M. V.; Wexler, A. S. Sulfur Speciation in Individual Aerosol Particles. *J. Geophys. Res. Atmospheres* **1996**, *101* (D13), 18701–18707. https://doi.org/10.1029/96JD01555.

(5) Whiteaker, J. R.; Prather, K. A. Hydroxymethanesulfonate as a Tracer for Fog Processing of Individual Aerosol Particles. *Atmos. Environ.* **2003**, *37* (8), 1033–1043. https://doi.org/10.1016/S1352-2310(02)01029-4.

(6) Dovrou, E.; Lim, C. Y.; Canagaratna, M. R.; Kroll, J. H.; Worsnop, D. R.; Keutsch, F. N. Measurement Techniques for Identifying and Quantifying Hydroxymethanesulfonate (HMS) in an Aqueous Matrix and Particulate Matter Using Aerosol Mass Spectrometry and Ion Chromatography. *Atmospheric Meas. Tech.* **2019**, *12* (10), 5303–5315. https://doi.org/10.5194/amt-12-5303-2019.

(7) Chapman, E. G.; Barinaga, C. J.; Udseth, H. R.; Smith, R. D. Confirmation and Quantitation of Hydroxymethanesulfonate in Precipitation by Electrospray Ionization-Tandem Mass Spectrometry. *Atmospheric Environ. Part Gen. Top.* **1990**, *24* (12), 2951–2957. https://doi.org/10.1016/0960-1686(90)90475-3.

(8) Schauer, A. J.; Kunasek, S. A.; Sofen, E. D.; Erbland, J.; Savarino, J.; Johnson, B. W.; Amos, H. M.; Shaheen, R.; Abaunza, M.; Jackson, T. L.; Thiemens, M. H.; Alexander, B. Oxygen Isotope Exchange with Quartz during Pyrolysis of Silver Sulfate and Silver Nitrate: Oxygen Isotope Exchange during Pyrolysis of Ag $_2$ SO $_4$ and AgNO $_3$. *Rapid Commun. Mass Spectrom.* **2012**, *26* (18), 2151–2157. https://doi.org/10.1002/rcm.6332.

(9) Geng, L.; Schauer, A. J.; Kunasek, S. A.; Sofen, E. D.; Erbland, J.; Savarino, J.; Allman, D. J.; Sletten, R. S.; Alexander, B. Analysis of Oxygen-17 Excess of Nitrate and Sulfate at Sub-Micromole Levels Using the Pyrolysis Method: Analysis of Oxygen-17 Excess of Nitrate and Sulfate. *Rapid Commun. Mass Spectrom.* **2013**, *27* (21), 2411–2419. https://doi.org/10.1002/rcm.6703.

(10) Jongebloed, U. A.; Schauer, A. J.; Cole-Dai, J.; Larrick, C. G.; Wood, R.; Fischer, T. P.; Carn, S. A.; Salimi, S.; Edouard, S. R.; Zhai, S.; Geng, L.; Alexander, B. Underestimated Passive Volcanic Sulfur Degassing Implies Overestimated Anthropogenic Aerosol Forcing. *Geophys. Res. Lett.* **2023**, *50* (1). https://doi.org/10.1029/2022GL102061.

(11) Kok, G. L.; Gitlin, S. N.; Lazrus, A. L. Kinetics of the Formation and Decomposition of Hydroxymethanesulfonate. *J. Geophys. Res.* **1986**, *91* (D2), 2801. https://doi.org/10.1029/JD091iD02p02801.

(12) Holt, B. D.; Kumar, R.; Cunningham, P. T. Oxygen-18 Study of the Aqueous-Phase Oxidation of Sulfur Dioxide. *Atmospheric Environ. 1967* **1981**, *15* (4), 557–566. https://doi.org/10.1016/0004-6981(81)90186-4.

(13) Dovrou, E.; Bates, K. H.; Moch, J. M.; Mickley, L. J.; Jacob, D. J.; Keutsch, F. N. Catalytic Role of Formaldehyde in Particulate Matter Formation. *Proc. Natl. Acad. Sci.* **2022**, *119* (6), e2113265119. https://doi.org/10.1073/pnas.2113265119.

(14) Broecker, W. S.; Oversby, V. M. *Chemical Equilibria in the Earth*; International Series in the earth and planetary sciences; McGraw-Hill: New York u.a, 1971.

(15) Bastrikov, V.; Steen-Larsen, H. C.; Masson-Delmotte, V.; Gribanov, K.; Cattani, O.; Jouzel, J.; Zakharov, V. Continuous Measurements of Atmospheric Water Vapour Isotopes in Western Siberia (Kourovka). *Atmospheric Meas. Tech.* **2014**, *7* (6), 1763–1776. https://doi.org/10.5194/amt-7-1763-2014.

(16) Holt, B. D.; Cunningham, P. T.; Engelkemeir, A. G.; Graczyk, D. G.; Kumar, R. Oxygen-18 Study of Nonaqueous-Phase Oxidation of Sulfur Dioxide. *Atmospheric Environ. 1967* **1983**, *17* (3), 625–632. https://doi.org/10.1016/0004-6981(83)90136-1.

(17) Liu, T.; Abbatt, J. P. D. Oxidation of Sulfur Dioxide by Nitrogen Dioxide Accelerated at the Interface of Deliquesced Aerosol Particles. *Nat. Chem.* **2021**, *13* (12), 1173–1177. https://doi.org/10.1038/s41557-021-00777-0.

(18) Shao, J.; Chen, Q.; Wang, Y.; Lu, X.; He, P.; Sun, Y.; Shah, V.; Martin, R. V.; Philip, S.; Song, S.; Zhao, Y.; Xie, Z.; Zhang, L.; Alexander, B. Heterogeneous Sulfate Aerosol Formation Mechanisms during Wintertime Chinese Haze Events: Air Quality Model Assessment Using Observations of Sulfate Oxygen Isotopes in Beijing. *Atmospheric Chem. Phys.* **2019**, *19* (9), 6107–6123. https://doi.org/10.5194/acp-19-6107-2019.

(19) He, P.; Alexander, B.; Geng, L.; Chi, X.; Fan, S.; Zhan, H.; Kang, H.; Zheng, G.; Cheng, Y.; Su, H.; Liu, C.; Xie, Z. Isotopic Constraints on Heterogeneous Sulfate Production in Beijing Haze. *Atmospheric Chem. Phys.* **2018**, *18* (8), 5515–5528. https://doi.org/10.5194/acp-18-5515-2018.

(20) Alexander, B.; Park, R. J.; Jacob, D. J.; Gong, S. Transition Metal-Catalyzed Oxidation of Atmospheric Sulfur: Global Implications for the Sulfur Budget. *J. Geophys. Res.* **2009**, *114* (D2), D02309. https://doi.org/10.1029/2008JD010486.

(21) Wang, X.; Gemayel, R.; Hayeck, N.; Perrier, S.; Charbonnel, N.; Xu, C.; Chen, H.; Zhu, C.; Zhang, L.; Wang, L.; Nizkorodov, S. A.; Wang, X.; Wang, Z.; Wang, T.; Mellouki, A.; Riva, M.; Chen, J.; George, C. Atmospheric Photosensitization: A New Pathway for Sulfate Formation. *Environ. Sci. Technol.* **2020**, *54* (6), 3114–3120. https://doi.org/10.1021/acs.est.9b06347.

(22) Savarino, J.; Thiemens, M. H. Analytical Procedure to Determine Both Δ18O and Δ17O of H2O2 in Natural Water and First Measurements. *Atmos. Environ.* **1999**, *33* (22), 3683–3690. https://doi.org/10.1016/S1352-2310(99)00122-3.

(23) Vicars, W. C.; Savarino, J. Quantitative Constraints on the 17O-Excess (Δ17O) Signature of Surface Ozone: Ambient Measurements from 50˚N to 50˚S Using the Nitrite-Coated Filter Technique. *Geochim. Cosmochim. Acta* **2014**, *135*, 270–287. https://doi.org/10.1016/j.gca.2014.03.023.

(24) Savarino, J.; Lee, C. C. W.; Thiemens, M. H. Laboratory Oxygen Isotopic Study of Sulfur (IV) Oxidation: Origin of the Mass-Independent Oxygen Isotopic Anomaly in Atmospheric Sulfates and Sulfate Mineral Deposits on Earth. *J. Geophys. Res. Atmospheres* **2000**, *105* (D23), 29079–29088. https://doi.org/10.1029/2000JD900456.

(25) Faust, B. C.; Anastasio, C.; Allen, J. M.; Arakaki, T. Aqueous-Phase Photochemical Formation of Peroxides in Authentic Cloud and Fog Waters. *Science* **1993**, *260* (5104), 73–75. https://doi.org/10.1126/science.8465202.

(26) Ye, C.; Chen, H.; Hoffmann, E. H.; Mettke, P.; Tilgner, A.; He, L.; Mutzel, A.; Brüggemann, M.; Poulain, L.; Schaefer, T.; Heinold, B.; Ma, Z.; Liu, P.; Xue, C.; Zhao, X.; Zhang, C.; Zhang, F.; Sun, H.; Li, Q.; Wang, L.; Yang, X.; Wang, J.; Liu, C.; Xing, C.; Mu, Y.; Chen, J.; Herrmann, H. Particle-Phase Photoreactions of HULIS and TMIs Establish a Strong Source of $H_2O_2$ and Particulate Sulfate in the Winter North China Plain. *Environ. Sci. Technol.* **2021**, *55* (12), 7818–7830. https://doi.org/10.1021/acs.est.1c00561.

(27) Harris, E.; Sinha, B.; Foley, S.; Crowley, J. N.; Borrmann, S.; Hoppe, P. Sulfur Isotope Fractionation during Heterogeneous Oxidation of SO&lt;Sub&gt;2&lt;/Sub&gt; on Mineral Dust. *Atmospheric Chem. Phys.* **2012**, *12* (11), 4867–4884. https://doi.org/10.5194/acp-12-4867-2012.

(28) Dominguez, G.; Jackson, T.; Brothers, L.; Barnett, B.; Nguyen, B.; Thiemens, M. H. Discovery and Measurement of an Isotopically Distinct Source of Sulfate in Earth's Atmosphere. *Proc. Natl. Acad. Sci.* **2008**, *105* (35), 12769–12773. https://doi.org/10.1073/pnas.0805255105.

(29) Au Yang, D.; Bardoux, G.; Assayag, N.; Laskar, C.; Widory, D.; Cartigny, P. Atmospheric SO2 Oxidation by NO2 Plays No Role in the Mass Independent Sulfur Isotope Fractionation of

Urban Aerosols. *Atmos. Environ.* **2018**, *193*, 109–117. https://doi.org/10.1016/j.atmosenv.2018.09.007.

(30) Sofen, E. D.; Alexander, B.; Kunasek, S. A. The Impact of Anthropogenic Emissions on Atmospheric Sulfate Production Pathways, Oxidants, and Ice Core Δ&lt;Sup&gt;17&lt;/Sup&gt;O(SO&lt;Sub&gt;4&lt;/Sub&gt;&lt;Sup&gt;2−&lt;/Sup&gt;). *Atmospheric Chem. Phys.* **2011**, *11* (7), 3565–3578. https://doi.org/10.5194/acp-11-3565-2011.

(31) Lyons, J. R. Transfer of Mass-Independent Fractionation in Ozone to Other Oxygen-Containing Radicals in the Atmosphere. *Geophys. Res. Lett.* **2001**, *28* (17), 3231–3234. https://doi.org/10.1029/2000GL012791.

(32) Anastasio, C.; Jordan, A. L. Photoformation of Hydroxyl Radical and Hydrogen Peroxide in Aerosol Particles from Alert, Nunavut: Implications for Aerosol and Snowpack Chemistry in the Arctic. *Atmos. Environ.* **2004**, *38* (8), 1153–1166. https://doi.org/10.1016/j.atmosenv.2003.11.016.

(33) Chu, L.; Anastasio, C. Formation of Hydroxyl Radical from the Photolysis of Frozen Hydrogen Peroxide. *J. Phys. Chem. A* **2005**, *109* (28), 6264–6271. https://doi.org/10.1021/jp051415f.

(34) Dubey, M. K.; Mohrschladt, R.; Donahue, N. M.; Anderson, J. G. Isotope Specific Kinetics of Hydroxyl Radical (OH) with Water ($H_2O$): Testing Models of Reactivity and Atmospheric Fractionation. *J. Phys. Chem. A* **1997**, *101* (8), 1494–1500. https://doi.org/10.1021/jp962332p.

(35) Lee, C. C.-W.; Savarino, J. H.; Cachier, H.; Thiemens, M. H. Sulfur (32S, 33S, 34S, 36S) and Oxygen (16O,17O,18O) Isotopic Ratios of Primary Sulfate Produced from Combustion Processes. *Tellus B* **2002**, *54* (3), 193–200. https://doi.org/10.1034/j.1600-0889.2002.01384.x.

(36) Harris, E.; Sinha, B.; Hoppe, P.; Foley, S.; Borrmann, S. Fractionation of Sulfur Isotopes during Heterogeneous Oxidation of SO&lt;Sub&gt;2&lt;/Sub&gt; on Sea Salt Aerosol: A New Tool to Investigate Non-Sea Salt Sulfate Production in the Marine Boundary Layer. *Atmospheric Chem. Phys.* **2012**, *12* (10), 4619–4631. https://doi.org/10.5194/acp-12-4619-2012.

(37) Yang, Y.; Weber, R. J. Ultrafiltration to Characterize PM2.5 Water-Soluble Iron and Its Sources in an Urban Environment. *Atmos. Environ.* **2022**, *286*, 119246. https://doi.org/10.1016/j.atmosenv.2022.119246.

(38) Anastasio, C.; Faust, B. C.; Rao, C. J. Aromatic Carbonyl Compounds as Aqueous-Phase Photochemical Sources of Hydrogen Peroxide in Acidic Sulfate Aerosols, Fogs, and Clouds. 1. Non-Phenolic Methoxybenzaldehydes and Methoxyacetophenones with Reductants (Phenols). *Environ. Sci. Technol.* **1997**, *31* (1), 218–232. https://doi.org/10.1021/es960359g.